1

Optical Architecture

The mission of a nanosatellite such as a CubeSat determines the instruments to be carried on board, commonly referred to as the "payload". Scientific observation missions based on electromagnetic radiation in the radio frequency to infrared range will determine its optical architecture. Optics are used in various types of instruments, such as altimeters, gyrometers, systems for optical telecommunications or metrology, atomic clocks in the case of service equipment, or equipment intended for observations and measurements in scientific experiments. This chapter is therefore devoted to instruments that use electromagnetic waves to probe the environment under study. It presents the various instruments that can be developed, namely high-spatial-resolution imagers with cameras, radiometers for measuring temperature fields, spectro-imagers with relatively low spatial and spectral resolutions used for remote sensing, reconnaissance and ground surveillance missions, spectrometers for measuring temperatures, pressures and water vapor content, LiDARs, active vertical sounders of the atmosphere for measuring the concentrations of constituents in the lower atmosphere (CO_2, CH_4, etc.) and telescopes for very high-resolution imaging. The distortions of these measuring devices are described, along with the optimizations needed to minimize them. Examples of implementations based on mission objectives are also provided.

1.1. Introduction

Artificial satellites have a wide range of applications: Earth observation using high-resolution imaging, medium-resolution imaging, meteorology and defense systems for societal, commercial and military activities. In research, examples include climate and environmental studies, oceanography, surface observations,

studies of the gravitational field and the Earth's magnetic field, and improving our knowledge of the universe, whether it be the solar system, stars, the interstellar medium, the galaxy or the distant universe.

In the field of optics, the applications of a satellite are those enabled by its onboard observation instruments. These instruments are based on the use of electromagnetic waves in the various domains of the electromagnetic spectrum that were presented and analyzed in Chapter 1 of Volume 1 (section 1.8.3):

> In the context of light-matter interaction, electromagnetic waves are used to study a physical-chemical system: molecules, materials, aerosols, atmosphere, environment. The properties and characteristics of matter can be analyzed by causing it to interact with electromagnetic waves (see Figure 1.21).
>
> Generally, the electromagnetic wave incident on the object is generated in a known state using a suitable source and filter system. In space, the Sun is often used as a light source. A detection system consisting of detectors and suitable filters is used to measure changes in the electromagnetic wave relative to its initial state at incidence. Studying changes in the characteristics of the reflected, transmitted, or scattered electromagnetic wave makes it possible to determine the properties of the system under study or its identification in case of absorption.

When observing a luminous object using an optical instrument, the latter is designed to increase our visual ability to see the details of image $A'B'$ of an object AB (see Figure 1.1) either by transmission through transparent materials or by reflection via mirrors. In this case, the structure of an optical system (see Figure 1.1) comprises an entrance pupil ($\mathbf{P_e}$) and an exit pupil ($\mathbf{P_S}$), characterized by their respective diameters, $\mathbf{D_e}$ and $\mathbf{D_s}$.

The function of such a system is to increase the angle α at which the object is seen from the entrance pupil by transforming the object into an image that will be seen at a larger angle α' from the exit pupil. The indicator or parameter characterizing the effect of the instrument is called the magnification G of the device. Its expression is given as:

$$G = \frac{\alpha}{\alpha'} = \frac{\left(\frac{A'B'}{O_S A'}\right)}{\left(\frac{AB}{O_{eA}}\right)} \qquad [1.1]$$

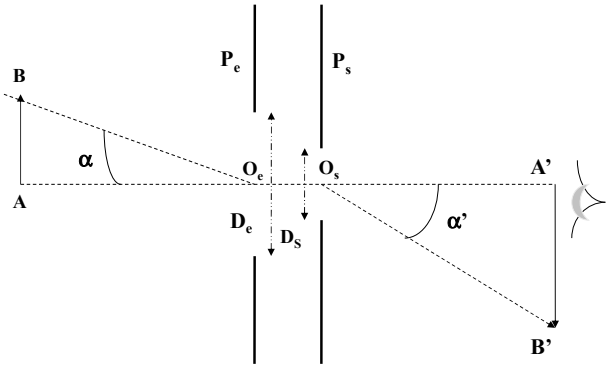

Figure 1.1. *Optical instrument for improving vision*

It should be noted that when the object is at infinity in the optical system, the size AB of the object is not defined and the magnification G is determined by the ratio of the angles, which are called the apparent diameter of the object and the image respectively: $G = \frac{\alpha}{\alpha'}$. Figures 1.2 and 1.3 show diagrams representing situations where the apparent diameters are determined to calculate the magnification using transparent materials, converging lenses characterized by their focal lengths f' (point of convergence of light from a very distant object through the lens).

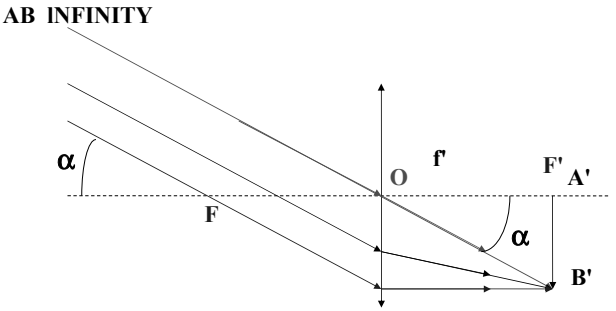

Figure 1.2. *Optical instrument for an object at infinity. For a color version of this figure, see www.iste.co.uk/dahoo/nanosatellites2.zip*

The angle α is given by $\alpha = \frac{A'B'}{f'}$.

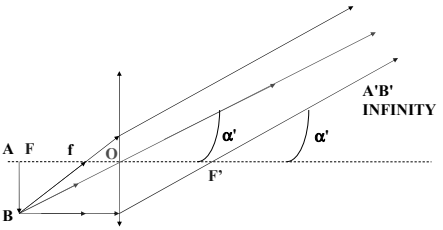

Figure 1.3. *Optical instrument for an image at infinity. For a color version of this figure, see www.iste.co.uk/dahoo/nanosatellites2.zip*

The angle α' is given by $\alpha = \frac{AB}{f}$.

An optical observation instrument consists of several essential components that work together to form a clear and detailed image of a distant or tiny object. Its design is a compromise between different parameters: magnification, resolution, brightness, field of view, etc. The choice of instrument will depend on the intended use. The optical architecture of a CubeSat-type nanosatellite is based on theories developed to understand and interpret light phenomena in the design of an instrument.

Chapter 5 provides an introduction to the development of science in the field of optics. It highlights scientific advances, which proceed by accumulation and correction, in a systemic approach, strongly emphasizing the questions, hypotheses and various interpretations that preceded the theories that are applied in the 21st century in the field of optics – in particular classical optics, which includes geometric optics and wave optics. Indeed, the use and data provided by a CubeSat will be subject to the same contexts of questioning, hypothesis formulation and various interpretations. Among these, it will be necessary to use the appropriate scientific approach to retain the most relevant and probable ones, which may evolve as knowledge advances.

This approach is understood through the lens of a history of science described from a Western perspective. It is presented in this way to remind us that all observations and data require, as Descartes explicitly stated in his *Discourse on the Method* [DES 37] (Volume 1, Chapter 2), a scientific methodology that "establishes the unification of the body of sciences on the critical examination of what a correctly directed mind allows, adjusting knowledge to the level of reason" (author's translation). The aim is to remind us that when analyzing data from onboard optical devices, we must try to minimize the erroneous assumptions and interpretations that punctuate the process of developing scientific knowledge, as the brief history of light phenomena shows.

It should also be remembered that scientific studies cannot be conducted independently of the socio-political-economic structure. Furthermore, constructive or destructive interference between belief and interpretation through logical deduction or induction influences scientific progress and can sometimes hinder its evolution. Indeed, as Harari [HAR 15] recounts in his book *Sapiens: A Brief History of Humankind*, in the fourth part devoted to the scientific revolution, in Chapter 14, "The Discovery of Ignorance":

> […] science is not an enterprise that takes place on some superior moral or spiritual plane above the rest of human activity. Like all other parts of our culture, it is shaped by economic, political, and religious interests.

In the same way that theories explaining the origin of planetary movements and their relative position in relation to the Sun have been developed over the centuries, as presented in Chapter 2 of Volume 1, with major contributions from Newton and Einstein, the understanding of light phenomena has evolved gradually. This evolution began with initial hypotheses that were only partially correct and has been progressively improved through the relentless work of many scientists, as described in Chapter 5 of this volume. It is therefore necessary to remember that the evolution of science has experienced periods of flourishing, periods of stagnation, and periods of regression throughout human history in order to better understand our future approach.

In this respect, the field of optics (light phenomena and vision) provides an exceptional field for highlighting the development of science through the accumulation and improvement of scientific knowledge. This has been achieved through the readjustment of hypotheses formulated throughout history, based on writings available since ancient times (–3,000 years) to the 21st century, where light phenomena are still the subject of research activities in terms of their nature, corpuscular and wave-like (dual nature of light), as well as quantum, such as the entanglement of photons. This approach allows us to better understand the phenomena of nature, observed with our senses and our technological sensors, which amplify our ability to comprehend the reality that surrounds us, as Descartes points out in the section "Optics, First Discourse: Of Light" of *Discourse on the Method* [DES 01]:

> All the management of our lives depends on the senses, and since that of sight is the most comprehensive and the noblest of these, there is no doubt that the inventions which serve to augment its power are among the most useful that there can be. And it is difficult to find any of these inventions augment the power of sight more than that of those

> marvelous telescopes which, in use for only a short time, have already revealed a greater number of new stars in the sky, and other new objects above the earth, than the sum total of those we have seen there before: so that, carrying our sight much farther than the imagination of our fathers was used to going, they seem to have opened the way for us to attain a knowledge of nature much greater and more perfect than our fathers had.

The design of nanosatellites and CubeSats fits into this vision of increasing our senses' ability to broaden our field of observation of space in order to expand our knowledge of nature.

Just like the laws of gravity, Newton's laws and methods developed in analytical mechanics are used to determine the orbital parameters and trajectory of satellites, while the laws of geometric optics are mainly used to develop optical instruments such as telescopes, astronomical binoculars, microscopes, spectrographs and spectrometers. However, when considering the resolving power of these devices, the principles of wave optics must be taken into account.

While an initial classification of the study of light-related phenomena in antiquity falls within the field of physiological optics and physical optics, modern optics focuses on the behavior and properties of light, light–matter interaction and the design of instruments to produce or detect light. The transition from physiological optics and physical optics to modern optics, via classical optics (geometric and wave optics), began at the end of the Middle Ages and has continued into the 21st century with quantum optics.

Figures 1.4(a) and (b) show respectively the covers by the same publisher of Witelo's or Vitellionis' work, which is a Latin translation of ancient works by Euclid and Ptolemy, written in Greek, and by Ibn Al-Haytham (Alhazen), written in Arabic, and that of Copernicus, who revolutionized the concepts of celestial mechanics with the heliocentric model. The covers of the works show an example of the transition from ancient and medieval concepts through illustrations of light phenomena and vision (see Figure 1.4(a)) and the works of those who contributed to the scientific revolution of the 7th century thanks to Copernicus' work on heliocentrism. These illustrations show, in Figure 1.4(a), the effect of a lens on rays that propagate in straight lines that are bent on the focal point, leading to heat and fire, the phenomenon of the rainbow distributed in a semicircle around the Sun-eye axis, the phenomenon of reflection in a mirror and the phenomenon of refraction on the optical illusion concerning the shortening and deformation of the legs of a person taking a bath.

a)

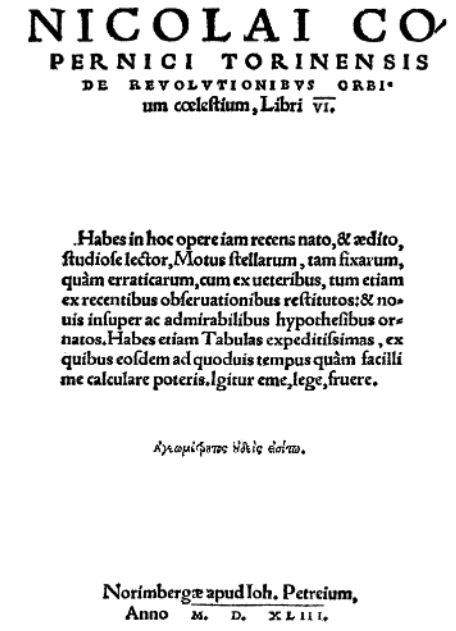

b)

Figure 1.4. *a) Vitellionis Mathematici Doctissimi, Peri Optikēs (source: Christie's). b) Nicolai Copernici De Revolutionibus (source: Wikimedia Commons)*[1]

The main theories that help us understand these phenomena are geometric optics (from antiquity and the Middle Ages to the 17th century), wave optics (from the 17th century to the 19th century), electromagnetism (from the 18th century to the 19th century), quantum optics and photonics (late 19th century and early 20th century to the present), as briefly presented in Chapter 1 of Volume 1. It should be noted that to interpret light–matter interaction, we use the framework of quantum mechanics and quantum electrodynamics, and that for the implementation of instruments in optical technologies, we can cite instrumental optics, photonics and quantum optics as the corresponding scientific fields.

1.2. Optical theories of light phenomena

The interpretation of light phenomena observed as a result of the interaction of the Sun, a natural source of light, with matter led to the theory of geometric optics.

1 See: https://thonyc.wordpress.com/2019/02/13/an-important-13th-century-book-on-optics/.

Examples include the mirage effect during the propagation of light in an inhomogeneous medium, the rainbow resulting from its reflection on water droplets, solar eclipses, the use of situations where the Sun is directly overhead for geometric calculations (circumference of the Earth) and the reflection of light on mirrors [BRU 65, BOR 99, HEC 05]. In geometric optics theory, light consists of rays grouped into a light beam. It propagates in a straight line in a homogeneous medium characterized by an optical index and follows Snell–Descartes' laws of reflection and refraction at the interfaces between two media with different optical indices.

However, if light is made to propagate through a very small opening, comparable to the wavelength of the light radiation, the phenomenon of diffraction can be observed. This phenomenon cannot be explained by geometric optics theory, as the light ray cannot be localized. It is necessary to rely on the approach developed by Huygens [HUY 90] and Fresnel [FRE 18], considering that light behaves like a wave. This is in accordance with the results obtained by Young [YOU 02] in his experimental work on interference and those of Grimaldi [GRI 65] on diffraction, which explain these phenomena. Note that the hypotheses of wave optics were later validated by the work of Maxwell [MAX 54, MAX 65].

The design of instruments for observing light phenomena is based on the laws of geometric optics. Examples include the telescope for astronomy, and the spectrometer for spectroscopic studies. These are optical systems with rotational symmetry about the optical axis, constructed using spherical mirrors (reflection: catoptric) and spherical lenses (refraction: dioptric). Before reaching the light detectors, the light beam must pass through apertures, which limits the optical range of the instrument.

In Volume 4 of the series "Infrared Spectroscopy", entitled *Infrared Spectroscopy of Symmetric and Spherical Top Molecules for Space Observation 2* [DAH 21b], Chapter 1 provides a description of optical instruments and spectrometers used to conduct observation campaigns of the Earth's atmosphere and laboratory experiments in the infrared domain. The four volumes in this series describe models based on the postulates of quantum mechanics. These models enable the interpretation of data from infrared space observations of homonuclear diatomic molecules (dihydrogen H_2, dioxygen O_2, dinitrogen N_2) or heteronuclear (carbon monoxide CO, hydrochloric acid HCl) [DAH 17a], linear triatomic molecules with axial symmetry (carbon dioxide CO_2, carbon oxysulfide OCS) and nonlinear molecules (water vapor H_2O, ozone O_3) [DAH 19], molecules classified as symmetrical spinning tops (ammonia NH_3) or spherical spinning tops (methane CH_4) in a gaseous environment, on the surface of ice or graphite, or in nanocages (clathrates, fullerene, rare gas matrix) [DAH 21c, DAH 21d].

In the series "Reliability of Multiphysical Systems", in Volume 2 [DAH 16] (*Nanometer-scale Defect Detection using Polarized Light*) and Volumes 9 and 10 (*Applications and Metrology at Nanaometer Scale 1 and 2*) [DAH 21a, DAH 21b], there is a description of the devices used to study matter at the volume level or at the surface level by polarized light spectroscopy or interference spectroscopy in the laboratory. There is also the theoretical background necessary for instrumental optics, such as geometric optics developed in matrix form, which allows the optical framework of instruments to be designed using software [3DO 24] or Huygens–Fresnel wave optics and Maxwell's electromagnetic waves for antenna design. These works provide a number of references for further study of the theoretical aspects of optics and waves in general.

There are two types of ray tracing simulation [3DO 24]:

– Sequential ray tracing: the optical elements are interconnected separately, one at a time, and light propagates from surface to surface in a predefined order. It is used to model the optical components of the optical system, define the optical properties of objects and represent light sources using directional rays, in order to then predict the behavior of the real system by observing the propagation of these rays through these optical system models.

– Non-sequential ray tracing: this approach allows for random and multiple connections between rays and surfaces through an automatic ray splitting procedure. Since non-sequential ray tracing allows rays to scatter and interact with the components of the optical system, which occurs naturally, this procedure allows users to better predict the actual behavior of optical systems than with the sequential ray tracing procedure.

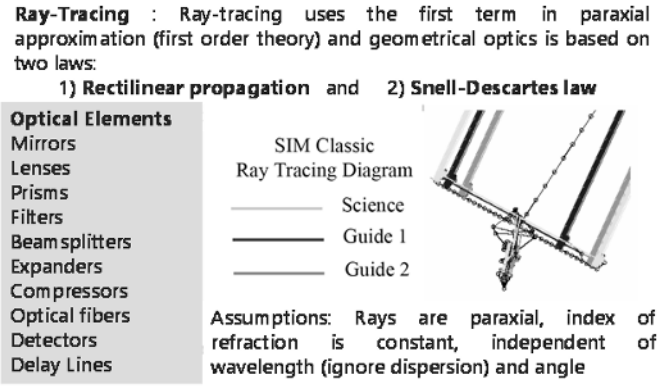

Figure 1.5. *Assumptions for ray tracing. For a color version of this figure, see www.iste.co.uk/dahoo/nanosatellites2.zip*

Figure 1.5 lists optical elements that can be used as components of an optical system. It summarizes the ray tracing assumptions and provides an example of a diagram obtained with SIM Classic.

Figures 1.6 and 1.7 summarize the fundamentals of geometric optics used in the design of instruments favoring reflection (R) or transmission (T). The difficulties that may arise from choosing R or T and the situations in which they are used are indicated, where possible. From an optical design and analysis perspective, mirrors (R devices) and lenses (T devices) are apertures (pupil, diaphragm) that limit the extent of light beams. Non-planar mirrors can be obtained by rotating a circle, an ellipse (prolate, oblate), a parabola and a hyperbola about an axis of symmetry (Volume 1, Chapter 2). The Schwarzschild parameter k ($k = -e^2$) is used for the algebraic equation giving the surface area.

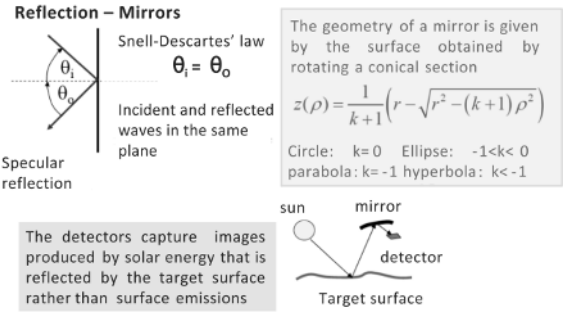

Figure 1.6. *Geometric optical elements for a reflection device*

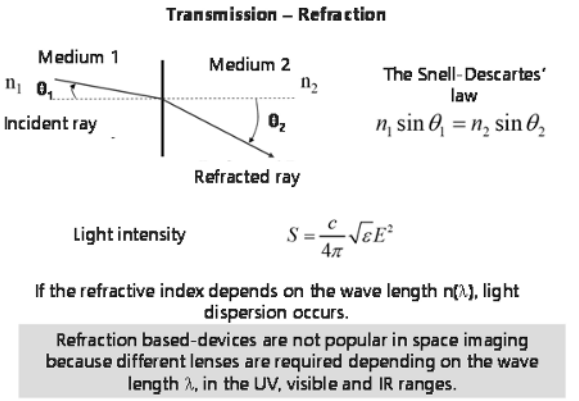

Figure 1.7. *Geometric optical elements for a transmission device*

Newton's corpuscular theory cannot explain the phenomena of interference and diffraction, nor can it correctly interpret the effect of a dense medium on the speed of light when it is refracted by the medium. However, Einstein's corpuscular approach (1905) [EIN 05], which assumes that light is made up of energy particles, later called photons, allows us to interpret the photoelectric effect. Light interacts with matter in the form of energy quanta: $E = h\nu$, where ν is the frequency associated with the color of light. In the case of the photoelectric effect, this is a phenomenon of induced absorption. Figure 1.8 summarizes the main quantities used to characterize light as a wave and a particle.

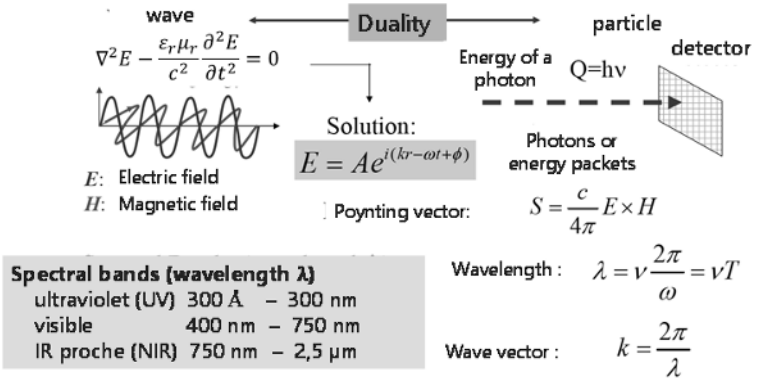

Figure 1.8. *Dual wave and particle properties of light. For a color version of this figure, see www.iste.co.uk/dahoo/nanosatellites2.zip*

By modeling a black body as sources radiating energy in discrete form, Planck solved the problem of the ultraviolet catastrophe of black body emission (note that the term "ultraviolet catastrophe" was formulated after Planck's theory of the black body emission in 1990). In 1915, Einstein explained black body emission by associating a symmetrical emission process with discrete absorption processes. Light can thus be considered as a wave or as a particle [DEB 68]. These different theories are further developed in more specialized works. The differences between classical sources (incoherent light) and quantum sources (coherent light) are shown using statistical theories of light. Concepts of quantum mechanics [MES 64, COH 73, MEI 15] are necessary to understand the corpuscular nature of light in the form of photons, as well as Glauber's formulation of light properties. All these theories are useful for understanding techniques that use polarized or unpolarized light to characterize matter and also to detect light.

The design and implementation of measurement instruments based on optical phenomena therefore require a good understanding of the concepts developed in geometric optics and wave optics. These concepts relate to the propagation of light rays, and in quantum physics, to the interaction between light and matter. A third element is the retrieval of measurement data by a suitable telecommunications system, which requires a good understanding of signal processing.

1.3. Optical systems for observation and detection

Observation and scientific missions rely mainly on optical architectures. An artificial satellite is an ideal observatory because it is not subject to the day/night cycle like ground-based observation instruments, nor to atmospheric effects (see Figure 1.9).

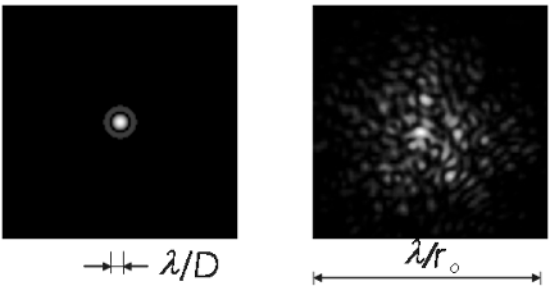

a) Diffraction b) Atmospheric turbulence

Figure 1.9. *The limits of ground-based observation. For a color version of this figure, see www.iste.co.uk/dahoo/nanosatellites2.zip*

As highlighted in section 1.8.3 of Chapter 1, Volume 1, the space sector distinguishes between the optical wave spectrum and the radio wave spectrum:

– Radio spectrum:

- microwave and radar → wavelengths from 1 mm to 10 cm;

- radio → wavelengths greater than 10 cm.

– Optical spectrum:

- gamma rays → wavelengths < 0.3 Å;

- X-rays → wavelengths from 0.3 Å to 100 Å;

- ultraviolet (UV) → wavelengths from 10 nm to 400 nm;

- visible (VIS) → wavelengths from 400 nm to 750 nm;

- violet (400–446 nm); blue (446–500 nm); green (500–578 nm);

- yellow (578–592 nm); orange (592–625 nm); red (625–750 nm);

- infrared → wavelengths from 0.76 μm to 500 μm.

The various instruments that can be developed within the framework of their optical component are as follows:

– high spatial resolution imagers with cameras (large pupil at the diffraction limit to provide sufficient light flux, long focal length, observation of small fields of view);

– radiometers (measurements of temperature fields on the surface of the object under study in order to analyze seasonal variations);

– spectro-imagers (with relatively low spatial and spectral resolutions) used for remote sensing, reconnaissance, and ground surveillance missions. These instruments have wide fields of view (90°). They can observe scenes from an altitude of 1,000 to 2,000 km (low-orbit satellites);

– spectrometers for measuring temperatures, pressures or water vapor content. These instruments have very high resolution and therefore a small angular field of view (requiring mechanisms to scan an observation);

– active vertical sounding of the atmosphere (LiDAR) to measure the concentrations of constituents in the lower atmosphere (CO_2, CH_4, etc.);

– telescopes for very high-resolution imaging.

Sunlight is most often used as a source of electromagnetic radiation by instruments used to observe the environment under study (except for LiDAR systems based on the scattering of laser light, for example). These instruments measure either the amount of light returned by reflection or scattering, or a spectroscopic property of an element in the environment – atom, molecule, charged particle or surface – that varies depending on the temperature, gravitational pressure, magnetic fields or composition of the environment. Whatever the case, these instruments need to have detection systems to record the measurements taken after the detectors are exposed to light.

Any analysis method requires the action of a probe (electromagnetic radiation, a beam of energetic particles, a magnetic field, a pressure field, a mechanical indentor, etc.) on a sample. This can be done experimentally in a laboratory or on the components of a medium in the space traversed by a CubeSat, for example. The result of the interaction between this probe and the material of the sample or medium may be another type of radiation, particles, a variation in the field detected by a series of measurements or even a law governing the behavior of the medium.

Figure 1.10 shows a schematic diagram of a lens-based astronomical telescope, such as the one made by Galileo, which enabled him to observe the moons of Jupiter [GAL 10].

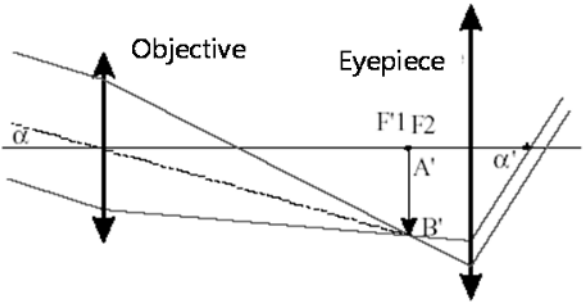

Figure 1.10. *Astronomical telescope based on lenses. For a color version of this figure, see www.iste.co.uk/dahoo/nanosatellites2.zip*

It is an optical system used to increase the apparent diameter of objects located at infinity and to increase the brightness of objects without apparent diameter, such as stars. It consists of a long focal length objective lens (f_1') and a short focal length eyepiece (f_2'). It is characterized by a magnification ($G = \frac{\alpha'}{\alpha}$) where α is the angle at which the observed object is seen with the naked eye at infinity and α' is the angle at which the virtual image ($A'B'$) given by the objective lens is seen through the eyepiece system. Given that α=A'B'/f'$_1$ and that α'=A'B'/f$_2$, the magnification G is given by: G = f'$_1$/f$_2$.

Figure 1.11 shows the basic diagram of a measuring device used to observe a medium's physical–chemical characteristics by probing it with a source of electromagnetic waves.

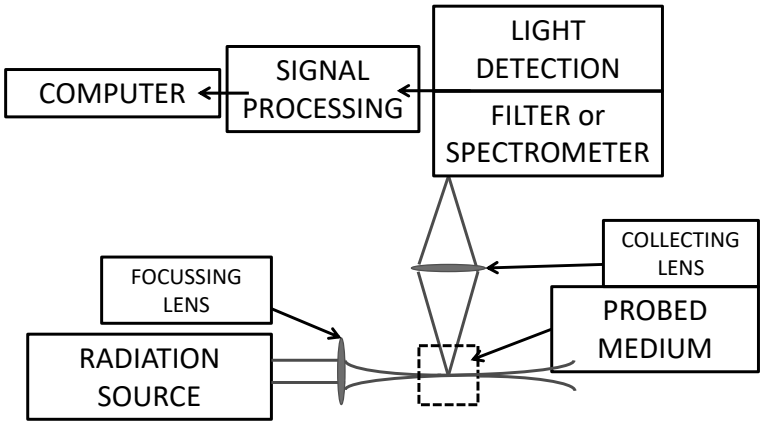

Figure 1.11. *Diagram of an observation-based measurement device. For a color version of this figure, see www.iste.co.uk/dahoo/nanosatellites2.zip*

Table 1.1 provides a non-exhaustive list of instruments typically carried on a space mission, as presented in Volume 1 (Chapter 1, Table 1.4).

Instruments	Functions	Orbit Type
Telescopes → Newtonian telescope → Two mirror telescope (Cassegrain, Ritchey-Chrétien) …	Mirror telescope for small field of view observation (few degrees) and high spatial resolution (few arcs) → Sun	Low Orbits Sun-synchronus Geostationary
Radiometers → Measurement of luminous flux emitted, scattered or reflected	Imaging and radiative balance	Low Orbits Sun-synchronus Geostationary
Lidars → Doppler (for velocity measurements) → Pulsed (for measurement of distances or of concentrations)	Measurement of concentrations and temperatures, detection of species (water vapor, CO2, …), measurement of velocity	Very Low Orbits Baloons Aircraft
Spectrometers → Vertical → Imager	Vertical sounding of atmosphere or multi-spectral imaging	Low Orbits Geostationary

Table 1.1. *Onboard observation instruments on missions*

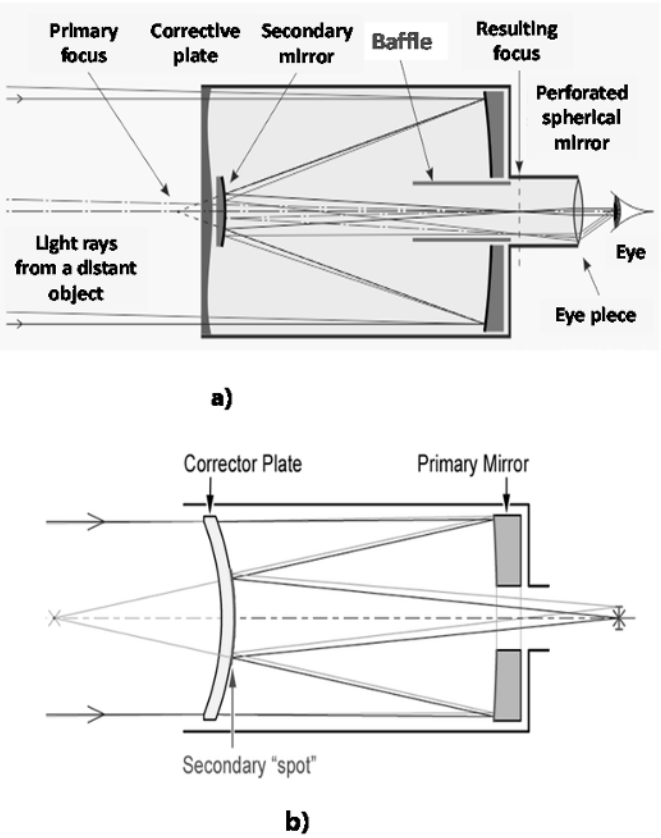

Figure 1.12. *Telescopes for space observation: a) Schmidt–Cassegrain (source: Serge Bertorello); b) Maksutov. For a color version of this figure, see www.iste.co.uk/dahoo/nanosatellites2.zip*

In the field of optics, such as the Ritchey–Chrétien telescope and the Czerny–Turner spectrometer (Volume 1, Chapter 1, Figure 1.10), space instruments dedicated to observing the Sun, which were given as examples of payloads in the first volume, all have various features in common. These instruments consist of a dispersion system to spread light into its spectral components (transmission, reflection or holographic diffraction grating, prism). They also include an entrance slit and an exit slit that limit the extent of the optical beam in the radiation paths and lead to diffraction phenomena and dispersion and astigmatism phenomena by refraction in a lens, for example. They may also present aplanatism if the object being viewed is extended.

The Schmidt–Cassegrain and Maksutov telescopes shown in Figure 1.12 and used for space observation are two additional examples that illustrate this point.

The detection system also consists of diaphragms, lenses or mirrors, which direct the radiation. These carry the useful information to a sensor system that converts electromagnetic energy into electrical energy, which is then transmitted to a reception center, as shown in Figure 1.13. The effect of the openings and materials used to direct light to the detectors must therefore also be taken into account.

It should be remembered that the main purpose of a telescope used for space observation is to ensure that images of observed space objects are as bright, contrasted and broad as possible. These characteristics define its three main functions, which are to collect as much light as possible, have the best possible resolution and provide the best possible amplification. Although these three functions are interdependent, they each have their own characteristics and limitations.

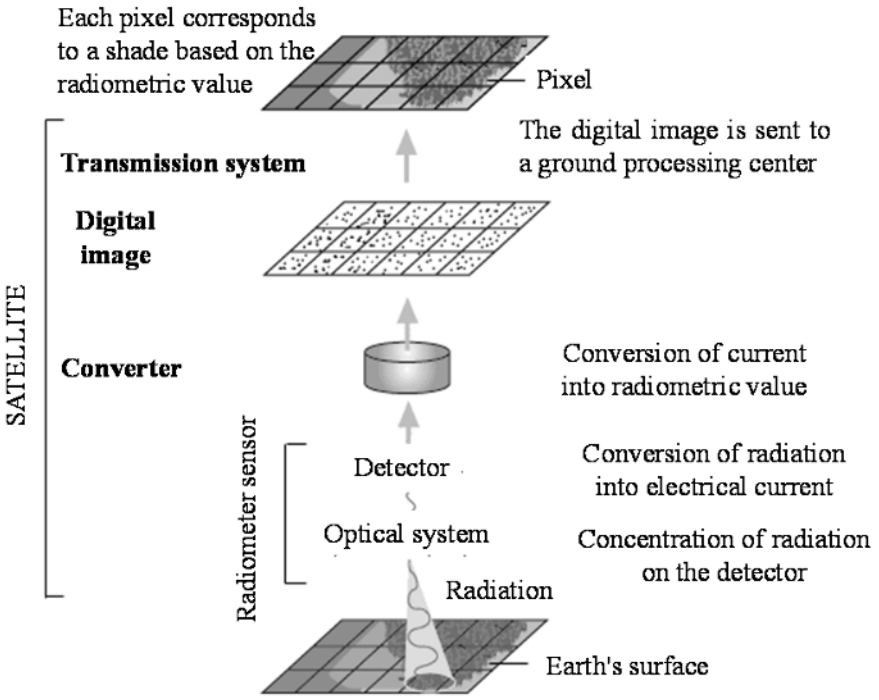

Figure 1.13. *Example of an image-based detection and observation system. For a color version of this figure, see www.iste.co.uk/dahoo/nanosatellites2.zip*

1.4. Main limitations of an optical system

The amount of light collected by a telescope depends mainly on the diameter of the aperture. However, it is the transmission path through the system that determines how much of the light collected at the entrance will actually reach the detection system. Transmission losses occur as a result of reflection, scattering and absorption of light, as well as obstacles and diaphragms in the light path. Resolving power determines the minimum size that can be resolved in the image reproduced from the observed object. In the absence of aberration, diffraction limits its resolution. Note that for images of two light sources to be completely resolved, they must be separated by at least one unilluminated photoreceptor or pixel [TEL 24].

1.4.1. *Resolution power and Rayleigh criterion*

In most optical instruments (microscopes, camera lenses, telescopes, etc.), observation is based on images. These instruments can be considered to have the role of forming images. From a theoretical point of view, geometric optics assumes that an instrument produces a point image (stigmatism) of an object. For example, with a microscope used to observe small objects, a set of lenses will produce a magnified image of an object illuminated by reflection or transmission before it is focused through a system of lenses and/or mirrors onto a CCD array.

In 1873, Abbe [ABB 73] used his mathematical theory of image formation through a microscope to show that the image of a point object cannot be a point (astigmatism phenomenon). He calculated a limit to the size of the observable object that depends on the resolution d of the device, which is expressed as follows:

$$d = 0.6\,\lambda/2nsin(\alpha) \qquad [1.2]$$

where the term $2nsin(\alpha)$ corresponds to the numerical aperture O.N. of the instrument and n is the refractive index of the medium in which the object is immersed. O.N. is expressed in terms of the maximum angle α between the optical axis and the rays emanating from the object viewed through the lens, at which the various emerging rays lead to the formation of the image of the object.

In wave optics, the image of a point does not lead to a point of light rays. Instead, it leads to a diffraction spot when the light emitted or scattered by the point source passes through a circular aperture whose radius is of the same order of magnitude as the wavelength of light, as observed in 1835 [AIR 35] by George Biddell Airy (1801–1892). This distribution of light after it passes through the circular aperture is called the Airy disk. The Airy disk consists of a bright central

disk surrounded by concentric rings that alternate between black and bright. It results from interference phenomena in the context of diffraction when light passes through the aperture characterized by its diameter *a*.

This is the same phenomenon that is responsible for the waist present in the Fabry–Pérot assembly used in a laser device, as described in Chapter 6 describing the specific characteristics of a laser source in nanotechnology [DAH 16, Figure 6.2]. The term diffraction to describe this light phenomenon was coined by Francesco Maria Grimaldi (1618–1663) in his posthumous work, *Physical Knowledge of Light, Colors, and the Rainbow*, published in Bologna in 1665 [GRI 65]. The theory for calculating diffraction phenomena was first proposed by Fresnel based on the principle stated by Huygens in his treatise on optics [HUY 90] to interpret the phenomenon of light according to wave theory, known as the Huygens–Fresnel principle, which Fresnel formulated as follows [FRE 18, BER 81]:

> Each point M on a surface Σ reached by light can be considered as a secondary source emitting a spherical wave. The vibrational state of this secondary source is proportional to that of the incident wave at M and to the surface element dΣ surrounding point M. The vibrations from the different secondary sources interfere with each other.

Following the work of Maxwell (1831–1879) on the propagation of an electromagnetic wave governed by a wave equation, as recalled in Appendix 1.8.3 (Volume 1, Chapter 1), Fresnel's calculations were reinterpreted as a mathematical boundary value problem by Kirchhoff (1824–1887). He neglected the vector nature of electromagnetic waves and considered light as a scalar quantity governed by Helmholtz's wave equation. Using Green–Ostrogradski's theorem, which allows us to move from a volume integral to a surface integral, we can show that Huygens–Fresnel's principle can be deduced from the Fresnel–Kirchhoff integral, as recalled in the appendix to the book *Applications and Metrology at Nanometer Scale 1* [DAH 21a], part of whose calculations are recalled in Appendix 1.8.3 (Volume 1). This calculation made it possible to introduce Fourier optics into the field of optical processing for observation instruments.

Figure 1.14 shows an example of the distribution of illumination in the image space as a result of Fraunhofer diffraction at large distances. The diffraction spot can be reduced to a finite distance by placing a converging lens between the slit and the screen, which is then located at the focal length *f* of the lens. In this case, $\sin\theta$ is replaced by ρ/f in the formula, giving the intensity distribution, where ρ is the distance to the center of the screen. Remember that the observation angle is measured relative to the optical axis of the system, which coincides with the mechanical reference axis (the sight-line viewing device) of the CubeSat or nanosatellite.

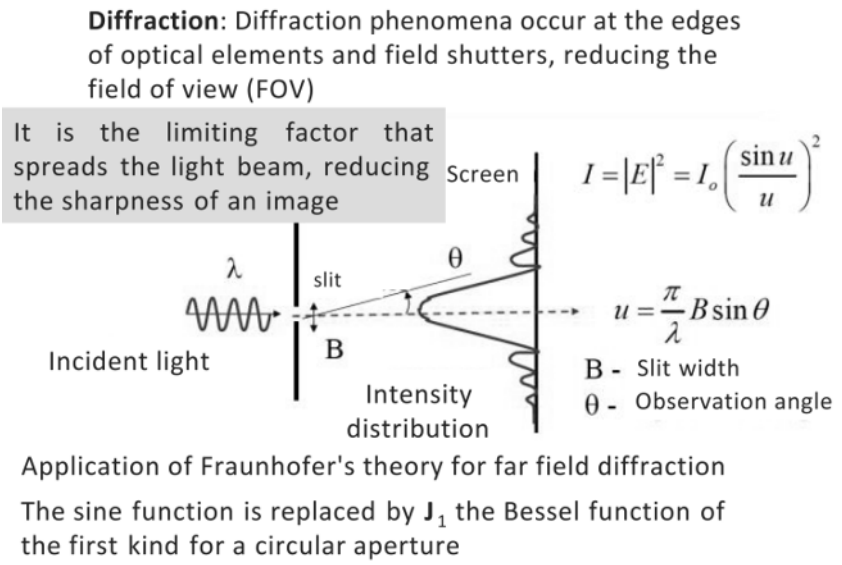

Figure 1.14. *Fraunhofer diffraction, a limiting factor in resolution*

The diffraction pattern for a pupil with diameter a, uniformly illuminated at a given wavelength λ, can be shown to be the Hankel transform of the transfer function of the optics, which leads to an illumination distribution $I(\alpha)$ (see Figure 1.15) in the focal plane of the instrument, revolving around the focus, and whose expression is given by:

$$I(\alpha) = \left[\mathcal{H} \left\{ \Pi \left(\frac{\alpha}{a} \right) \right\}_{q=\alpha/\lambda} \right]^2 = \left[\frac{\lambda a J_1\left(\frac{\pi a \alpha}{\lambda}\right)}{2\alpha} \right]^2 \quad [1.3]$$

where $\alpha = sin\theta$ (see Figure 1.14), and J_1 represents the Bessel function of the first kind (see Figure 1.15).

The initial light beam gives rise to a diffraction pattern (see Figure 1.15) that corresponds to the distribution of light on the observation screen as a function of an angle θ, expressed in reduced units u, for an aperture diameter a and a wavelength λ. The first zero of the diffraction pattern is located at 3.83, which gives an Airy pattern characterized by an angular width given by $\sin\theta = 1.22\lambda/a$ when the illumination is incoherent.

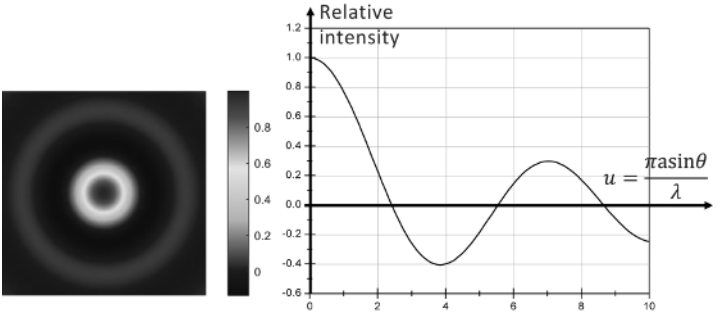

Figure 1.15. *Light diffracted by a circular diaphragm: intensity as a function of u. For a color version of this figure, see www.iste.co.uk/dahoo/nanosatellites2.zip*

In the visible range of the electromagnetic spectrum, resolution is limited to 200 nm. However, Abbe believed that this limit could be overcome with advances in technology and our understanding of physical phenomena. This resolution limit is Rayleigh's criterion (1842–1919), associated with half the wavelength λ of the radiation used for observation. According to this criterion, two images are just hardly separated when the central maximum of one figure coincides with the first minimum of the other. The critical angular separation between two sources according to this criterion is written at small angles as: $\theta_c = \frac{1.22\lambda}{a}$, corresponding to the Airy disk and the situation shown in Figure 1.16(b).

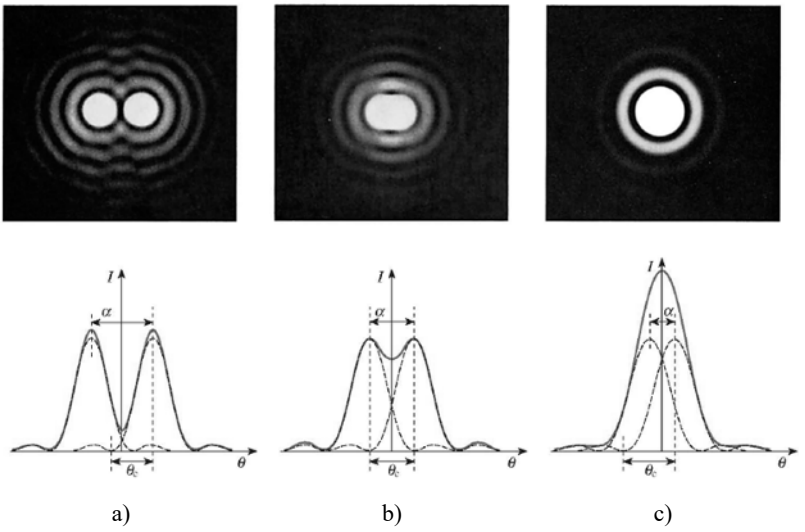

Figure 1.16. *Illustration of the Rayleigh criterion*

Figure 1.17 shows a situation that satisfies Rayleigh's criterion for a given configuration of two objects observed on a distant screen through a circular aperture with diameter a.

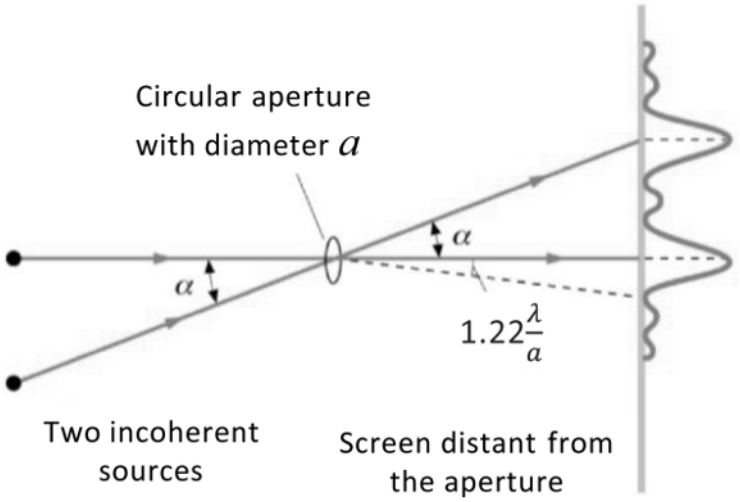

Figure 1.17. *Resolution limit based on the Rayleigh criterion*

Figure 1.18 gives two examples of the application of Rayleigh's criterion in the observation of an object by the eye. In Figure 1.18(a), the task is to determine the limiting angle of resolution of the eye for an entrance aperture of diameter $a = 2.00\ 10^{-3}$ m and visible radiation of wavelength $\lambda = 500\ 10^{-9}$ m. The limiting angle of resolution is calculated to be $3\ 10^{-4}$ radians.

In Figure 1.18(b), the aim is to determine the minimum separation *d* between two point sources that the eye is capable of distinguishing if they are located at the *punctum proximum* (pp), i.e. at a distance $L=25\ 10^{-2}\ m$ from the eye for an entrance aperture of diameter $a = 2.00\ 10^{-3}$ m and visible radiation of wavelength $\lambda = 500\ 10^{-9}$ m. The minimum separation *d* is calculated to be approximately $7.5\ 10^{-5}$ m.

The diameter of an optical system will determine the size of the spacecraft. In Figure 1.19, we calculate a value of 117 m for the smallest lunar crater that can be resolved by the Hubble telescope with an aperture diameter of 2.4 m, for visible radiation of wavelength $\lambda = 600\ 10^{-9}$ m and a distance of $3.84\ 10^{8}$ m. The angular resolution or resolving power of the telescope is its ability to clearly separate or resolve two point sources (distinct Airy discs).

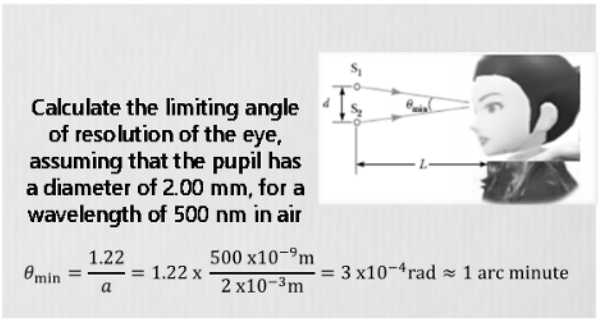

Figure 1.18. *The resolving power of the eye*

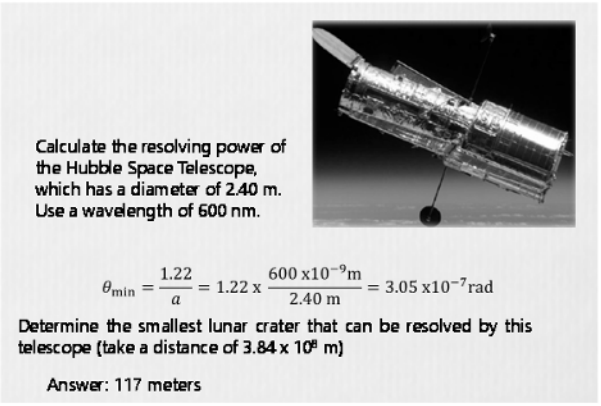

Figure 1.19. *The resolving power of the Hubble telescope*

The systems for collecting and transmitting RF (radio frequency) signals and optical signals are identical in theory. However, the physical device is different. In principle, an optical mirror is equivalent to a disc-shaped RF parabolic antenna. The detection system is placed at the focal point of the main lens of the optical/RF system, as shown in Figure 1.20.

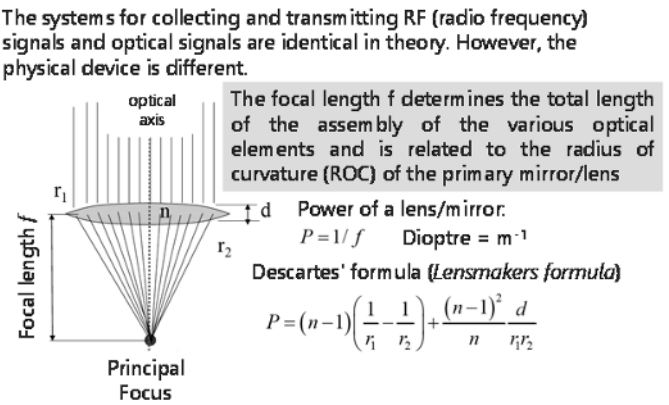

Figure 1.20. *The optical mirror is equivalent to the RF parabolic antenna*

The focal length f is used to determine the length of the optical assembly consisting of all the optical elements. It is determined experimentally after measurement. Descartes' formula (lensmakers formula) can be used to evaluate this value numerically. Two methods can be used to determine the focal length. They are summarized in the flowcharts shown in Figures 1.21 and 1.22. The first method requires knowledge of the field of view (FOV) and the size of the image in the observation plane. Remember that in the case of an optical instrument or sensors, this is the solid angle through which a detector is sensitive to light or electromagnetic radiation. Appendix 2.7.1 of Chapter 2 reviews the concepts of solid angle in the case of surface emissivity and object luminance.

With the first method, we use a magnification formula given by:

$$\frac{f}{h} = \frac{r_d}{R} \qquad [1.4]$$

where f is the focal length in m, h is the altitude in m, r_d is the radius of the detector array and R is the radius of the target in m.

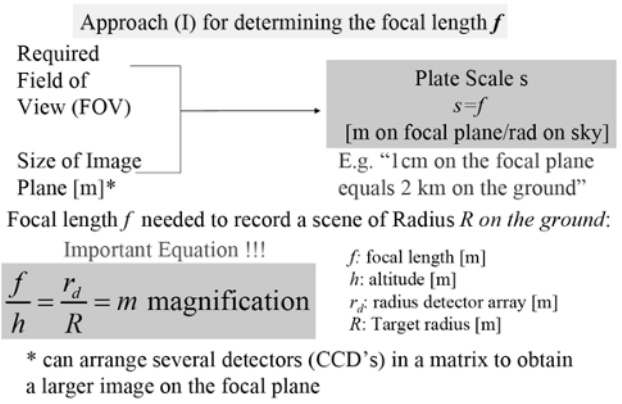

Figure 1.21. *Approach 1: procedure for measuring focal length. For a color version of this figure, see www.iste.co.uk/dahoo/nanosatellites2.zip*

With the second method, target points arranged at fixed distances are detected and the following formula is used:

$$f = \frac{\Gamma D}{2{,}44\lambda} \qquad [1.5]$$

where f is the focal length in m, D is the diameter of the aperture in m, λ is the wavelength of the detected radiation in m and Γ is the diameter of an image at a target point in m. This formula is obtained from the diameter of the Airy disc: $d_{AIRY} = \frac{2{,}44\lambda}{D}$.

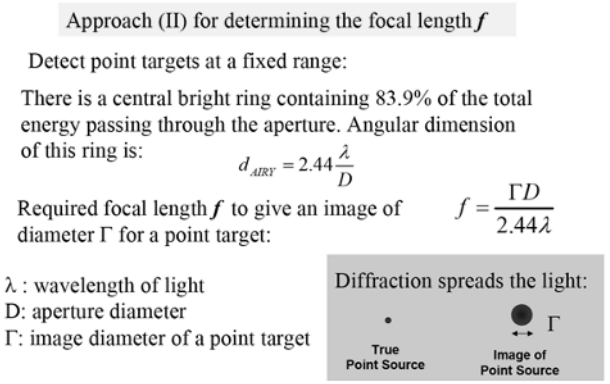

Figure 1.22. *Approach 2: procedure for measuring focal length*

A telescope is characterized by a number of parameters, as shown in Figure 1.23. The main functions of a telescope are: adequate brightness of the observed object, sufficient resolving power and the highest possible magnification given the resolution.

Most important: **f** - Focal length $F\# = \frac{f}{D} = \frac{1}{2NA}$

Infinity F-number*, e.g. F# or f/

* a.k.a. F-stop: synonyms: f/, F, F No., F#

Numerical Aperture $NA = \frac{1}{2F\#} = \frac{D}{2f}$

Image brightness is proportional to $1/F^2$

Depth of focus δf: $\frac{1}{f} = \frac{1}{h} + \frac{1}{f + \delta f}$

Best optical systems are DIFFRACTION-LIMITED.

Figure 1.23. *Characteristics of a telescope*

In remote sensing, the solid angle (see Appendix 2.7.1 of Chapter 2) through which a detector element (a pixel sensor) is sensitive to electromagnetic radiation at a given moment is called the *instantaneous field of view* or IFOV. The spatial resolution of a remote sensing imaging system is often expressed in terms of the dimensions of the visible ground area for a known sensor altitude. The single-pixel IFOV is closely related to the concepts of *resolved pixel size*, resolved ground distance, ground sampling distance and modulation transfer function [WIK 24b].

Just like in remote sensing, when a telescope is pointed towards space to observe a distant star, for example, or towards Earth to measure the brightness of a surface being scanned, the spatial resolution is expressed in terms of the ground resolution distance based on a number of parameters. These include the distance to the ground, the visible surface being scanned and other characteristics of the telescope, as shown in Figure 1.23. The diagram in Figure 1.24 summarizes an observation situation that depends on the focal length f of the telescope and the altitude h.

The dotted rays originate from the ends of the target on the assumed flat Earth's surface and pass through the ends of the limited circular aperture of the focusing lens with diameter D. The solid rays also originate from the ends of the target, but pass through the center of the lens to converge on the array of detectors. The red dotted line passing through the center of the lens defines the optical axis of the observation

system. The distance between the intersection of this line on the array and the image of the extreme point of the target on the array defines the radius r_d of the target image. The pixel (picture element) corresponding to the resolution Δx defines the resolution of the image on the detection system.

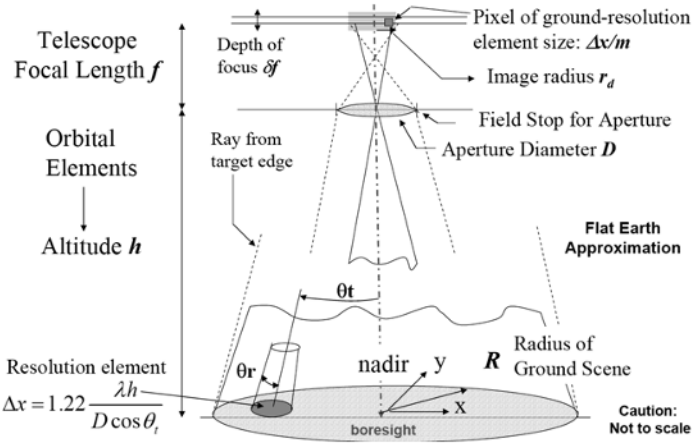

Figure 1.24. *Observation of deep space through a telescope. For a color version of this figure, see www.iste.co.uk/dahoo/nanosatellites2.zip*

The ground resolution (see Figure 1.24) is determined by the angular resolution given by Rayleigh's diffraction criterion: $\theta_r = 1.22\frac{\lambda}{D}$ (see Figure 1.16), for a circular aperture. Let R_0 be the distance between the center of the observation lens and the abscissa x on the target. For an angle θ_t, this gives $h = R_0 cos\theta_t$ and $x = R_0 sin\theta_t$, which is the length perpendicular to the axis of vision. We therefore calculate the variation $\Delta x = R_0 cos\theta_t \Delta\theta_t = h\theta_r$ for a variation of $\Delta\theta_t = \theta_r$. The elements involved in acquiring data corresponding to a target with radius R observed at nadir (the point in the sky directly below an observer, opposite the zenith) at altitude h lead to a resolution power $\Delta x = 1.22\frac{\lambda h}{D}$ depending on the length perpendicular to the axis of vision relative to the axis of the CubeSat (boresight axis).

We can use the approximation $\Delta x = R_0\theta_r = 1.22\frac{\lambda h}{Dcos\theta_t}$. This formula is related to the ground resolution of 0.3 m, which is specified in the SOW (statement of work: a document that legally binds a subcontractor and the main project sponsor). Note that in astronomical imaging, angular resolution is the correct metric for the resolution indicator, because the target is generally a distant star with low luminosity (point source: order of magnitude 1 arcsec = 4.8 μradians).

The field of view (FOV) in astronomy is generally expressed as an angular area seen by the measuring instrument or telescope in degrees to the square, or for high-magnification instruments in arcminutes to the square. The angle is measured in the sky relative to the Earth in general. Based on the diagram in Figure 1.24, the FOVs can be determined as shown in Figure 1.25.

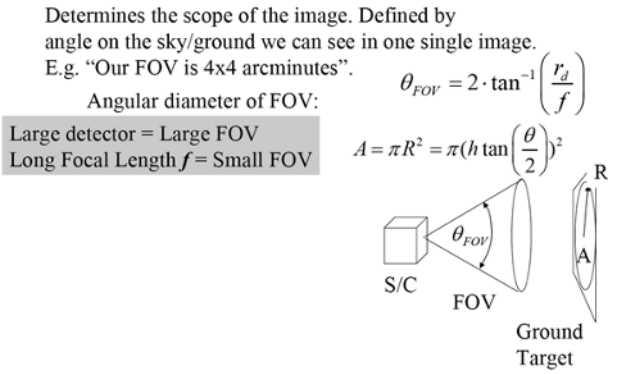

Figure 1.25. *Field of view (FOV)*

For reference, the wide-field channel of the Advanced Camera for Surveys on the Hubble Telescope has a field of view of 10 arcminutes to the square, and the high-resolution channel of the same instrument has a field of view of 0.15 arcminutes to the square. Ground-based survey telescopes have much wider fields of view [WIK 24b].

1.4.2. *The defects of a real optical instrument*

An optical instrument is an assembly of lenses, mirrors or both. These are often systems centered on a rotational symmetry axis that coincides with the optical axis. Their function is to produce an *extended image* of *extended objects* in terms of illumination (an object is a set of point light sources, just as an image is a set of image points). Devices are classified as *objective* instruments and *subjective* instruments. In the former, which are projective devices, *real images* are obtained on photographic plates, CCDs or a screen (projection lantern, camera, eye, etc.), and in the latter, which are ocular instruments, *virtual images* are obtained (glasses, telescope, magnifying glass, microscope, etc.). Ideally, an optical system produces a flat image perpendicular to the optical axis from a flat object perpendicular to that axis. In reality, optical devices are not perfect and do not necessarily operate under Gaussian conditions (Gaussian optics), with light rays substending a small angle with respect

to the optical axis. In reality, the image is distorted by the presence of diaphragms and by the dispersion of light in a transparent material.

Optical aberrations are observed, which are factors that limit image quality. These include chromatic aberrations, spherical aberrations, coma, astigmatism and field curvature.

If the Gauss conditions (Gaussian optics) are not met, geometric spherical defects are observed. In the presence of lenses, chromatic defects are observed. This is because the index of a material varies depending on the color and material, which disperses polychromatic light into its components, as is the case with white light. Figure 1.26 shows an example of chromatic aberration in the case of a converging lens.

There is a dispersion of colors, with the corresponding beams converging at different focal points on the optical axis.

Figure 1.27 shows three cases of image distortion due to geometric aberration.

In the image plane, when the light rays coming from the object, which is in the form of a grid (the red dotted lines on the diagonals are used to locate the object in relation to the image), are limited by the presence of diaphragms, depending on the position of the diaphragms, we observe barrel distortion, pin-cushion distortion or no distortion.

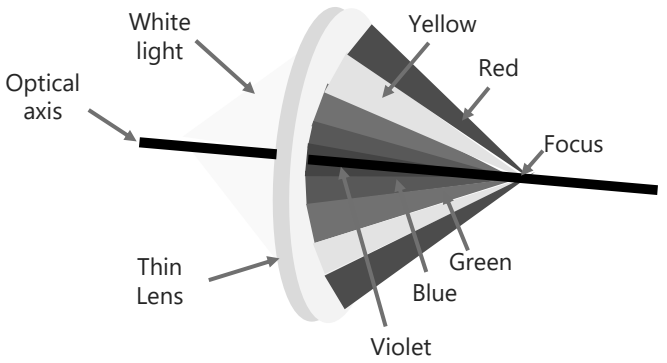

Figure 1.26. *Axial chromatic aberration of a converging lens. For a color version of this figure, see www.iste.co.uk/dahoo/nanosatellites2.zip*

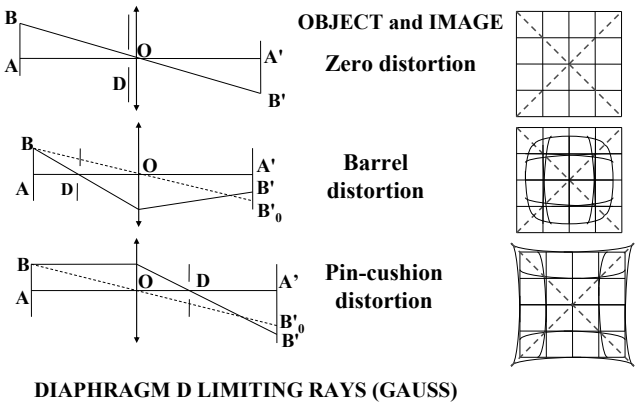

Figure 1.27. *Image distortion due to geometric aberration*

Another type of aberration concerns the sphericity of the lens present in the optical system (see Figure 1.28).

When object A is at infinity, we observe in the image space that image point A'_0 is at image focus F'_0 for paraxial rays, and that image point A'_m is at focus F'_m for marginal rays. We refer to λ_p and τ_p as the spatial domain corresponding to longitudinal and transverse spherical aberrations respectively.

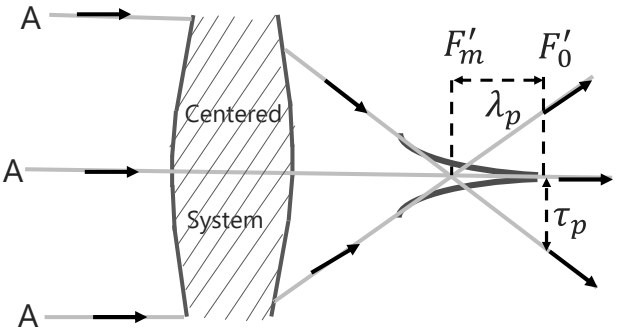

Figure 1.28. *Distortion due to geometric spherical aberration. For a color version of this figure, see www.iste.co.uk/dahoo/nanosatellites2.zip*

Figure 1.29 shows the types of defects present in spherical aberration. The curved surface behind the lens, denoted ΩΣ, is the wavefront of the light.

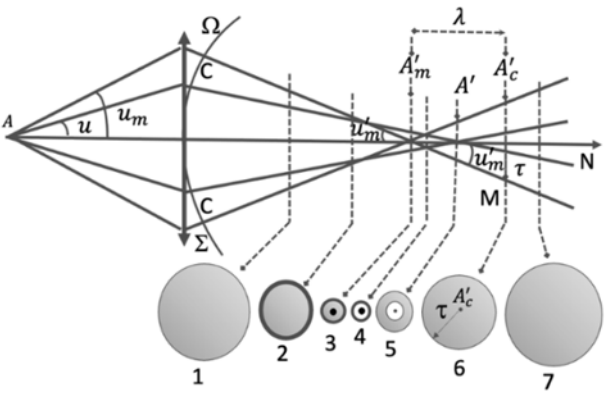

Figure 1.29. *Distortion due to geometric spherical aberration. For a color version of this figure, see www.iste.co.uk/dahoo/nanosatellites2.zip*

All incident rays with the same inclination u form a cone of revolution with vertex A on the axis from which the rays originate. The emerging rays form a cone of revolution with vertex A' on the axis (u varies from 0 to u_m). When u varies from 0 to u_m, A′ moves from A'_0 to A'_m, where A'_0 is the image for central or paraxial rays (Gaussian optics) and A'_m is the image of marginal rays. The convergence of a thin lens increases with u. It is more convergent for marginal rays. When a screen is moved perpendicular to the optical axis, the different aspects of the emerging beams can be observed: for example, 4 is not a point image, as there is an accumulation of light, and 6 is the best image of ray $\tau = A'_0 M$ (Gaussian optics). If the aperture is limited by diaphragming the incident beam, λ and τ, which characterize the aperture aberration for object point A, decrease ($\tau/\lambda=\tan(u'_m)$). The parameters λ and τ measure the longitudinal and transverse spherical aberrations respectively.

Spherical aberrations can be corrected by limiting the edges of the lenses (aperture diaphragm), favoring non-spherical lenses (difficult to manufacture, rarely used), or combining lenses with different curvatures (doublet, triplet). The disadvantage is that this results in a decrease in contrast and resolution (blurred image).

1.4.2.1. *Summary of the various defects and their processing*

– *Chromatic aberration:* associated with refracting telescopes that use lenses as objectives. This is a defect of lenses that cannot bring light beams with different wavelengths to the same point of convergence. The result is an image with a faintly

colored halo (usually purple) around bright stars, planets and the Moon. This aberration also reduces lunar and planetary contrast. It becomes more apparent as apertures increase and speeds increase. These defects can be reduced by using achromatic doublets and even virtually eliminated by more expensive and sophisticated designs, such as apochromats or those incorporating fluorite lenses.

– *Spherical aberration:* has the effect of converging light rays passing through lenses or reflected by mirrors at different distances from the optical axis towards different positions on the axis. This causes images of point stars to appear blurred in the form of a disc rather than a point image. Most telescopes are designed to avoid this defect.

– *Coma:* mainly associated with parabolic reflectors, which affect images located off axis and are more pronounced at the edges of the field of view. The images observed have a V-shaped appearance. The higher the focal ratio (ratio of focal length to aperture diameter), the more visible the coma will be near the edges. However, the center of the field (approximately a circle, which in mm is the square of the focal ratio) is free of coma in well-designed instruments.

– *Astigmatism:* this is a lens aberration that elongates images, which change from a horizontal position to a vertical position on either side of the best focus position. It is generally associated with poor-quality optics and collimation errors.

– *Field curvature:* this is an effect caused by light rays that do not all converge at the same focal point in the same plane. The center of the field may be well defined and located at the focal point, but the edges are not located at the focal points, or vice versa (see Figure 1.26).

The existence of optical aberrations causes a phase shift (delay or advance) at certain points on the wavefront of a light beam. This phase shift depends on the degree of optical aberration causing these defects, which limits the transfer of the object's characteristics to its conjugate image. The analysis of the wavefront surface is performed using a Fourier transform and Zernike polynomials [GAV 15]. Thus, optical aberrations can be simulated as a combination of Zernike polynomials (see Figure 1.30) to represent the wavefront of light. Certain classic optical aberrations (defocus, coma, etc.) are correlated with one of the first Zernike polynomials, while higher-order aberrations correspond to polynomials of strictly higher degree than 2. Thus, using Zernike polynomials and Seidel coefficients, the effects of spherical aberration and coma can be simulated, as shown in the form of surface distribution of light in Figure 1.30, which makes it possible to anticipate the type of defects that are likely to degrade images.

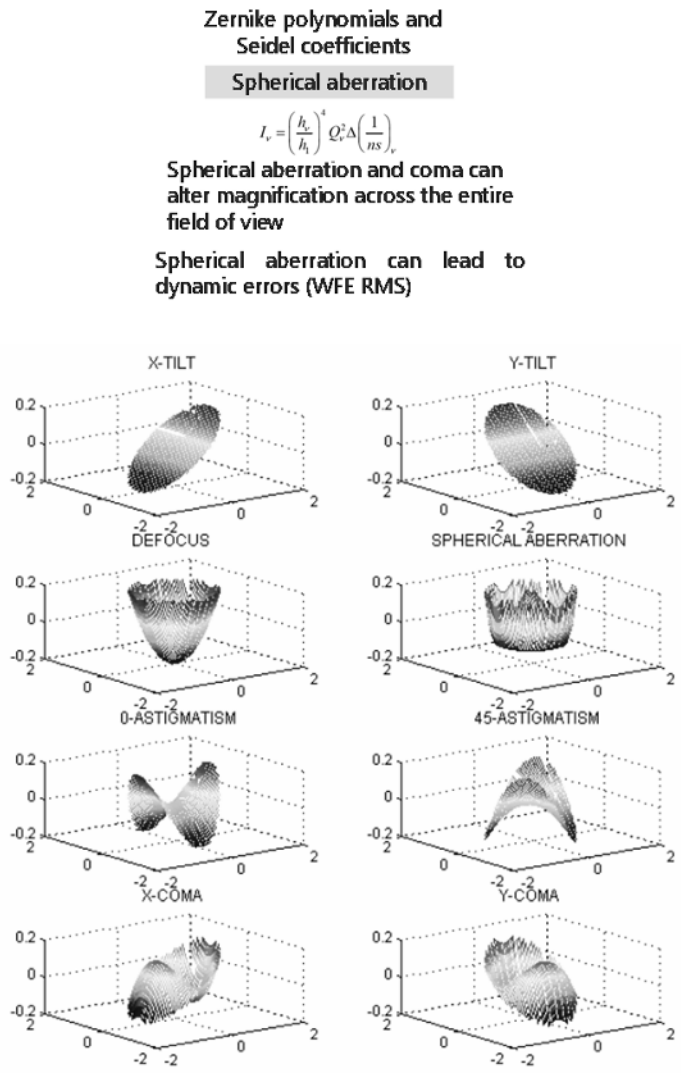

Figure 1.30. *Simulation of the effects of spherical aberration and coma. For a color version of this figure, see www.iste.co.uk/dahoo/nanosatellites2.zip*

1.4.3. *Fourier optics and the spatial frequencies of an object*

In Fourier optics, an image is a two-dimensional signal that can be broken down into its spatial frequencies in each of its two dimensions (Appendix 1.8.1.1). The

image can be reconstructed using its spatial spectrum if the phase of each component is known precisely:

– The cutoff frequency represents the highest spatial frequency that the optics can transmit. Beyond that, the instrument no longer transmits.

For a given entrance pupil diameter (D), wavelength (λ), angular aperture of the optics (α') and focal length (f), we have:

$$v_c = \frac{D}{\lambda} \text{ in cycles per radian or } v_c = \frac{2\,\alpha'}{\lambda} = \frac{D}{\lambda\, f} \text{ in cycles per meter}$$

– The Nyquist frequency represents the spatial frequency defined by half the sampling frequency of the pixels on the ground level.

– The maximum frequency to be used is that specified by the user.

The optical transfer function, or OTF, of an optical system is a complex function that relates the luminance in the space of the object to the illuminance in the space of the image. It allows the influence of the optical system on the distribution of light energy in the image space to be modeled. Although the optical transfer function is often considered only in the conjugate object and image planes, it is three-dimensional. It is decomposed into an amplitude known as the *modulation transfer function* and a phase known as the *phase transfer function*.

The phase transfer function (PTF) characterizes the phase shifts introduced by the optical system. It is particularly relevant in the near field, assuming Fresnel diffraction.

The modulation transfer function (MTF) characterizes the optical system's ability to reproduce contrast based on the fineness of the object's details, which corresponds to its ability to transmit the object's spatial frequencies. It is used to evaluate the quality of the optical system in the field of photography and cinematography. It represents the attenuation and phase shift of the spatial frequencies of the object. To determine the MTF, measurements must be made. This test provides a synthesis of the contrast and resolution of an optical system. It is based on the observation of a test chart (see Figure 1.31) composed of alternating white and black lines that become increasingly narrow. The white lines are slits that allow light to pass through, while the black lines are opaque.

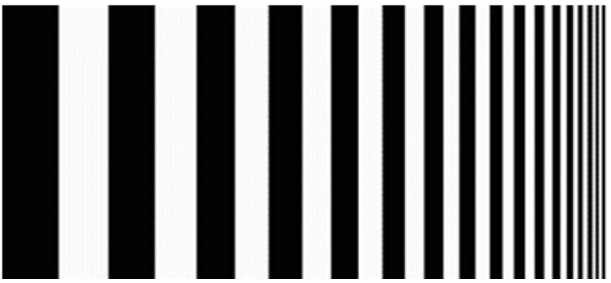

Figure 1.31. *Simple classic test chart used to evaluate the MTF of an optical system such as a lens*

In practice, a system is said to be limited by diffraction if the aberrations affecting it have a point spread function that is smaller than the Airy disc created by diffraction. The point spread function of an optical system, meaning the image of an object point, is a three-dimensional illumination distribution that has a maximum in the conjugate plane of the object plane. This function corresponds to the two-dimensional Fourier transform of the aperture shape ([1.33] in Appendix 1.8.1.1). The optical transfer function is then expressed as the autocorrelation product of the aperture shape, as follows:

$$\widehat{H}_1(\nu_x, \nu_y) = \gamma_t t(\lambda D_i \nu_x, \lambda D_i \nu_y) \otimes t(\lambda D_i \nu_x, \lambda D_i \nu_y) \qquad [1.6]$$

where γ_t is the transverse magnification, $\otimes$ denotes the convolution operation and D_i is the distance to the plane where the image is formed.

The maximum frequencies recorded by the imaging system are limited by:

– the optical system due to the diffraction effect;

– the sensor due to the size of the pixels.

In many cases, if the object is far enough, the image is considered to be formed in the vicinity of the focal plane, so that $D_i = f'$.

The theoretical diffraction-limited MTF for an instrument with a circular aperture is determined after calculating the optical transfer function. In the case of an optical system with an image focal length f′ and equipped with a circular entrance pupil of diameter d, the parture number (or F-number) is denoted by N = f/d. We also consider that the image is formed in the vicinity of the focal plane, so that $D_i \cong f'$.

The symmetry of the problem allows the normalized optical transfer function to be expressed as a function of spatial frequencies along any radial axis of the aperture, such as (see the calculation example for a circular aperture):

$$\widehat{H}_1(\nu) = \frac{2}{\pi}\left(arccos\left(\frac{\nu}{\nu_c}\right) - \frac{\nu}{\nu_c}\sqrt{1-\left(\frac{\nu}{\nu_c}\right)^2}\right) \quad [1.7]$$

where the cutoff frequency, beyond which there is no longer any contrast, is given by $\nu_c = \frac{1}{\lambda N}$.

1.4.3.1. *Calculation example for a circular aperture*

The transmission function of a circular aperture is given by $t(X,Y) = 1$ $for\ \sqrt{X^2+Y^2} \leq \frac{d}{2}$ $and\ is\ 0\ otherwise$. From formula [1.6], we can evaluate the autoconvolution (or autocorrelation with two same objects) of $t(X,Y)$. Since the function is real and even, we determine the intersection area of the two discs (see Figure 1.32) as follows:

$$\sqrt{(\lambda D_i \nu_x)^2 + \left(\lambda D_i \nu_y\right)^2} \leq \frac{d}{2} \quad [1.8]$$

This leads to a maximum radius ν_{max} given by:

$$\sqrt{(\nu_x)^2 + \left(\nu_y\right)^2} = \nu_{max} \leq \frac{d}{2\lambda f'} \quad [1.9]$$

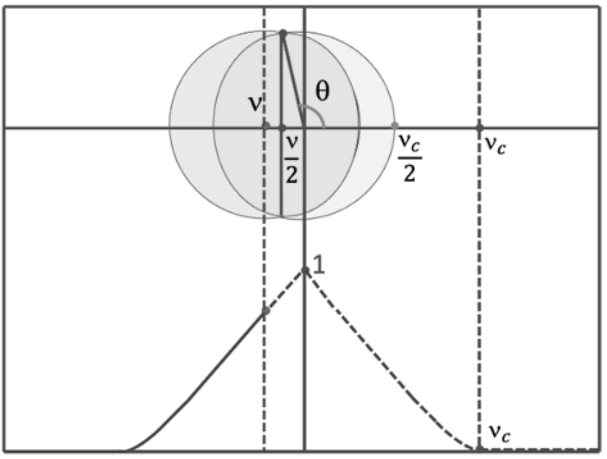

Figure 1.32. *Case of the autoconvolution of a circular aperture. For a color version of this figure, see www.iste.co.uk/dahoo/nanosatellites2.zip*

As shown in Figure 1.32, there is a cutoff frequency ν_c beyond which the discs no longer overlap, and the autoconvolution function becomes zero. We calculate ν_c as follows:

$$\nu_c = 2\nu_{max} = \frac{d}{\lambda f'} = \frac{1}{\lambda N} \quad [1.10]$$

When the discs intersect, given the symmetry of revolution, we can simply study any axis of the disc (along a diameter). We consider positive frequencies $\nu > 0$. By parameterizing the positive angles by the angle θ, as shown in Figure 1.31, such that $cos(\theta) = \frac{\nu/2}{\nu_c/2} = \frac{\nu}{\nu_c}$, and calculating the area as that of two symmetrical circular segments subtended by the angle 2θ, we obtain the following result:

$$A = 2\left(\frac{(\nu_c/2)^2}{2}\right)(2\theta - 2sin2\theta) \quad [1.11]$$

This leads to the following expression:

$$\mathrm{A} = 2\left(arccos\left(\frac{\nu}{\nu_c}\right) - \frac{\nu}{\nu_c}\sqrt{1 - \left(\frac{\nu_c/2}{\nu_c}\right)^2}\right) \quad [1.12]$$

since $cos(\theta) = \frac{\nu}{\nu_c}$ and $sin(\theta) = \sqrt{1 - \left(\frac{\nu_c/2}{\nu_c}\right)^2}$.

At its maximum, the area is $A_{max} = \pi(\nu_c/2)^2$, and normalizing by A_{max}, we obtain expression [1.7].

It should be noted that the MTF of an optical system obviously depends on the aperture and its shape, as well as on the wavelength due to diffraction. However, other phenomena also contribute to its degradation. Most geometric and chromatic aberrations that affect the optical system, in addition to manufacturing or handling defects, reduce the MTF values. We must therefore address the effects of spherical aberration, coma aberration, astigmatism, field curvature and trefoil (clover-shaped image).

Internal reflections within the optical system can reduce the MTF across the entire image by decreasing contrast due to flare. Vignetting and distortion do not affect the MTF. Chromatic aberrations do not affect the MTF in quasi-monochromatic light. The distance to the object can change the optical aberrations present in the optical system and modify the MTF associated with it. The polarization of the incident light can, on rare occasions, have an influence. Therefore, it is necessary to develop optical systems to correct images in certain situations, as shown in Figure 1.33.

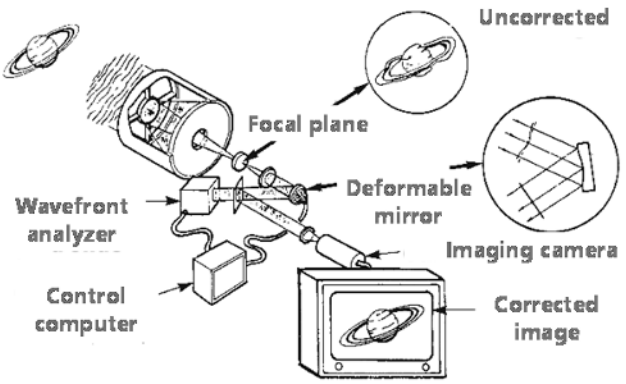

Figure 1.33. *Systems for image correction*

1.5. Light detection system in an optical system

Like the human eye and photographic plates, devices for detecting photons rely on the interaction between light and matter. The device generates charge carriers as a result of this interaction. In astronomy, photon counting systems are preferred in the visible part of the spectrum. Their principle is based on the energy intensification of incident photons through photon–electron conversion by the photoelectric effect. The technology to be implemented depends on the use of photoelectrons (multiplication and/or acceleration) and the target used for detection (phosphor, photodetectors, resistive or conductive anodes, etc.).

These different devices differ, regardless of their technical characteristics, in terms of their readout mode: parallel, serial or instantaneous. Parallel readout provides excellent dynamic range, but for a very limited number of pixels (< 500). Serial readout allows for refocusing, but limits dynamic range, unlike instantaneous readout. Dead time effects, which determine the dynamics of a detection system, must be taken into account in the detection system.

The purpose of an onboard or ground-based astronomical camera is to obtain images of luminous objects in the sky, regardless of their brightness and the distance between the camera and the object being viewed.

There are different types of sources in the solar system, either direct emitters such as the Sun, or indirect emitters such as the Moon or planets – although CO_2 fluorescence has been observed on Earth from Mars due to induced emission. Due to their great distances outside the Solar System, galaxies/nebulae are very dim,

sometimes barely brighter than the black sky in the background. In this case, it is necessary to expose for a long time so that enough photons reach the observation camera's sensor. In addition to the brightness/luminance ratio of the final image, it is also necessary to evaluate the influence of signal-to-noise ratios on the quality of the recorded image.

1.5.1. *Poynting vector and photon detection*

The electromagnetic field of a light wave has an electric component **E** and a magnetic component **B** perpendicular to each other, while also being perpendicular to the direction of propagation of the wave. The Poynting vector **S** of a wave represents the power carried per unit area, and its time average is expressed as follows:

$$\vec{S} = \frac{1}{2}\left(\vec{E} \wedge \vec{H}^*\right) \qquad [1.13]$$

where $\left|\vec{H}\right| = \frac{\vec{E}}{Z_0}$ and Z_0 is the characteristic impedance of the medium, which in a vacuum is equal to $\sqrt{(\mu_0/\varepsilon_0)}$. The Poynting vector is parallel to the direction of wave propagation in a homogeneous isotropic medium.

The energy carried by a wave is detected by placing the surface of a detector perpendicular to the path of the wave (see Figure 1.34).

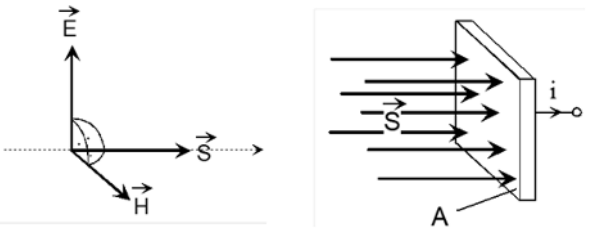

Figure 1.34. *Modeling light detection using the Poynting vector*

The total power P carried by the wave and detected on a surface A is given by:

$$P = \oiint \vec{S}\vec{n}dxdy = \frac{1}{2Z_0}\oiint\left|\vec{E}\right|^2 dxdy = \frac{A}{2Z_0}\left|\vec{E}\right|^2 \qquad [1.14]$$

which leads to a quadratic detector. If we denote the detector response by R, the photocurrent is given by:

$$i = RP = R\frac{A}{2Z_0}\left|\vec{E}\right|^2 = K\left|\vec{E}\right|^2 \quad [1.15a]$$

Since the intensity I of light is given by $I = \varepsilon_0 c\left|\vec{E}\right|^2$, we finally calculate:

$$i = RP = K\left|\vec{E}\right|^2 = R\frac{A}{2}I \quad [1.15b]$$

Detection is therefore a nonlinear process.

Let W be the energy incident on the detector. The number n of photons incident on the detector is given by $n = \frac{W}{W_{ph}} = \frac{W}{h\nu}$. The total charge is equal to $q = \eta e\frac{W}{h\nu}$, where η is the detection efficiency.

The photocurrent is therefore given by:

$$i = \frac{dq}{dt} = \frac{\eta e}{h\nu}\frac{dW}{dt} = \frac{\eta e}{h\nu}P = R_0 P \quad [1.15c]$$

1.5.2. *Semiconductor-based detectors, photodiodes and CCDs*

Photon detection is the result of light–matter interaction. Photons incident on the surface of a semiconductor are absorbed and generate charge carriers (holes and electrons) that induce a photocurrent (photoelectric effect). This absorption is also accompanied by heat emission, as part of the light energy is converted into heat. Figure 1.35 shows the characteristics of a semiconductor-based photon detector.

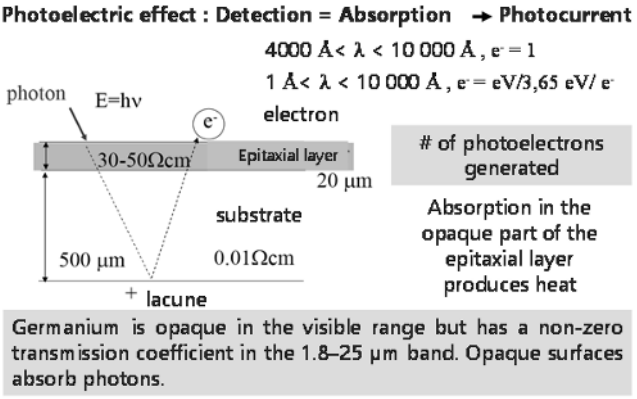

Figure 1.35. *Characteristics of a semiconductor-based sensor*

1.5.2.1. *CCD – characteristics*

For remote detection, CCDs (charge-coupled devices) are used (see Figure 1.36). Most CCDs exploit a field effect: a dielectric film covers the doped layer, and transparent electrodes are connected to this film. Charge carriers (usually electrons, but sometimes also "holes") accumulate on the film. Another thin conductive layer is sometimes inserted between the pixels to improve contrast and electrically discharge overexposed pixels.

Incident light transfers its energy to the electrons in the semiconductor through the internal photoelectric effect. This transfer releases electrons (with a negative charge) and "holes" (with a positive charge), which repel each other when an electrical voltage is applied. Unlike what happens with a photodiode, the charges are not immediately discharged, but accumulate in a memory cell, a potential well, which operates as a capacitor. If it is decoded in time, before the photodiode reaches voltage saturation, the total charge stored is proportional to the exposure.

A CCD photographic sensor is a charge-coupled device. In document scanners and many other similar applications, the devices are linear; they move transversely over the object to be scanned. In cameras and digital video cameras, the sensors are grouped together on a rectangular surface, where each CCD forms a line, often in the smallest dimension of the image (2,028 vertically and 1,014 horizontally).

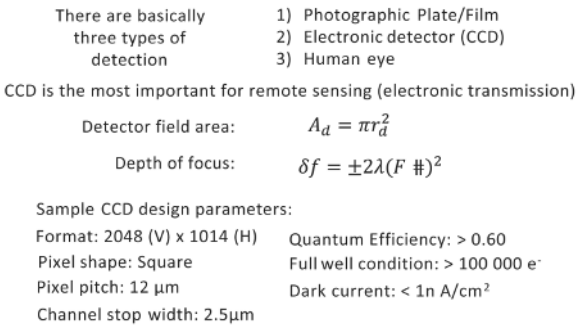

Figure 1.36. *Features of a CCD-based sensor*

Each photosensitive element charges one of the CCD elements in proportion to its illumination. The exposure is then suspended while a clock signal causes the charge to be transferred to the neighboring element, ultimately serializing the information.

It should be noted that very low-noise CCDs are used for photon counting applications limited to very low signal-to-noise ratios. These are applications requiring

fast, low-noise reading. The number of pixels reached when detecting radiation depends on the field of view.

1.5.2.2. *CCD – sensitivity*

The size of a pixel is given by:

$$d = (2\theta_r f)Q = \frac{2.44\lambda f}{D}Q \qquad [1.16]$$

where Q, the quality factor, is set to ½ to avoid undersampling.

The field of view depends on the number of pixels.

Rather than the total amount of signals in an image, which depends on the gain in the camera's electronics, sensitivity is the signal-to-noise (S/N) ratio obtained for a given exposure time. The S/N ratio is a measure of quality: the higher the ratio, the less grainy the image will be.

It should be noted that:

– in clear weather, a distant object in the sky corresponds to at least 25 S/N;

– narrower pixels (9 µm) require a longer exposure time (lower sensitivity);

– in dark or cloudy weather, a distant object in the sky can be oversampled;

– larger pixels (24 µm) require a shorter exposure time for undersampling if the source is bright or has high luminance.

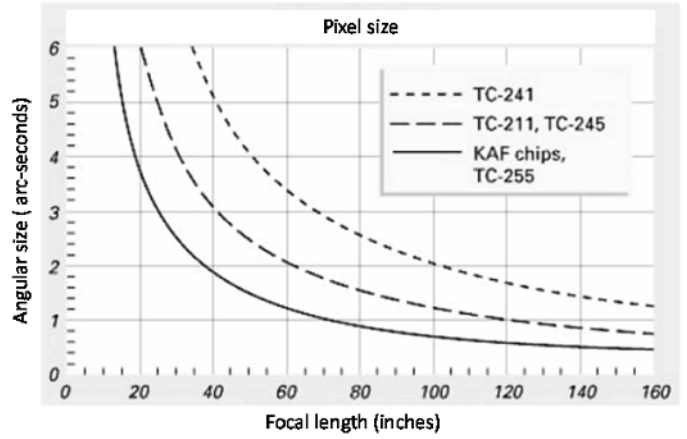

Figure 1.37. *Angular coverage depending on focal length*

The efficiency of a sensor element is expressed as the number of electrons produced per photon received. The larger the surface area of an element, the more photons it receives, and therefore the higher the light sensitivity and dynamic range of the CCD. However, as the number of elements decreases for a given length, a larger sensor and a lens of longer focal length are required (see Figure 1.37) to maintain resolution.

In cases of overexposure or when bright objects saturate the CCD, the charges in one memory cell can influence those in a neighboring cell as a result of excess charges along a column of pixels. An anti-blooming circuit, which functions as a drain and clips excess energy, can reduce or eliminate this effect. For long exposure times, the output signal is no longer proportional to the exposure. This procedure can cause side effects, such as increased dark currents and reduced sensitivity. For this reason, this practice is avoided in scientific applications of CCD sensors.

After exposure, the charge transfer device functions as a bucket chain to the output filter. The sensor output signal is transmitted in series: each pixel's charges are transmitted one after the other, whereas incident light charged them simultaneously, "in parallel", during exposure. The main characteristics of CCD chips are as follows:

– *Quantum efficiency:* this is proportional to the probability that an incident photon will give rise to an electron [CRO 14]. It depends on the wavelength of the light and can exceed 90% (see Figure 1.38) (compared to a photographic film: 5–10%). The quantum efficiency of a CCD sensor describes its response as a function of the wavelength of the incident radiation. Standard sensors designed for front illumination, for example, are more sensitive to green, red and infrared (500–800 nm) than they are to blue (400–500 nm) radiation. CCDs designed for back illumination have exceptional quantum efficiency compared to those designed for front illumination (see Figure 1.38).

– *Dark current in photosensitive cells:* this depends heavily on temperature and, due to its statistical properties, causes *sui generis* noise, which affects each pixel differently and is a source of digital noise. It is also a source of "hot pixels", in other words pixels affected by high dark current.

– *Full well capacity:* this is the amount of charge that a pixel can store, or the depth of the potential well, which can be very high. This ensures a high dynamic range in the sensor's response to incident radiation.

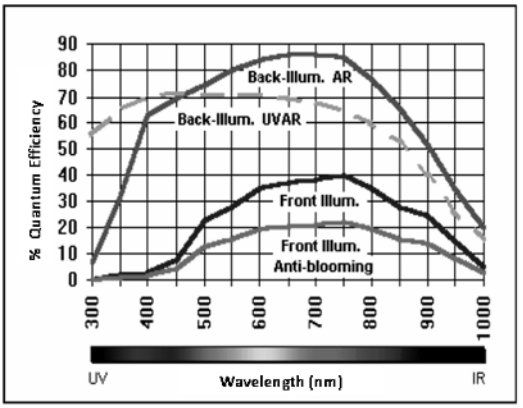

Figure 1.38. *Quantum efficiency as a function of wavelength. For a color version of this figure, see www.iste.co.uk/dahoo/nanosatellites2.zip*

– *The behavior of individual cells in the event of overexposure:* in the event of overexposure, the cells receive more charges than they can store. When the charge influences neighboring pixels, blooming occurs, which manifests itself as a bright streak on the image. This phenomenon is called smear. One way to deal with this situation is to use a special circuit (anti-blooming gate) to divert excess charges, which is found in many digital cameras. However, these circuits sometimes discharge certain cells prematurely, causing some useful information to be lost, which destroys the linearity of the relationship between illumination and charge, and degrades the relationship between the image and the object, reducing the accuracy of the measurement.

– *Efficiency:* the efficiency achieved by transferring the charge to the output filter is very favorable compared to sensors based on other principles.

– *Noise factor:* background noise from the output filter (decoding noise, readout noise).

In high-resolution cameras, dark current and noise levels are limited by cooling the chip. Using liquid nitrogen, dark current can be reduced to less than three electrons per pixel per hour.

– *Advantages of a CCD detector in astronomy:*

- allows the detection of very faint stars due to the high sensitivity of the CCD detector;

- provides access to a wide range of the detection spectrum;

- provides a higher dynamic range (i.e. the ability to effectively contrast tiny sources of very bright objects within the same image);

- allows data containing recorded information to be digitized, which is a great advantage in photometry for analysis and storage, and for the development of complex image processing algorithms.

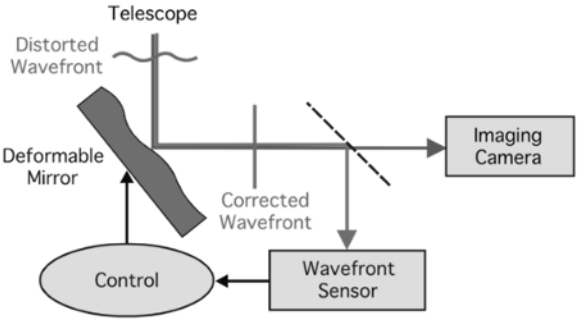

Figure 1.39. *Wavefront correction using a deformable mirror. For a color version of this figure, see www.iste.co.uk/dahoo/nanosatellites2.zip*

– *Detection optimization:* measuring devices can incorporate wavefront correction devices. These compensate for image distortions caused when light travels through a layer of the atmosphere using adaptive optics with a deformable mirror, as shown in Figure 1.39.

1.6. Application examples

Reducing the size of a satellite to CubeSat standards (multiples of 1 U up to 24 U) requires a rethink of payload design within the optical architecture. This section shows two examples of technical considerations to be taken into account for upcoming CubeSat missions following UVSQ SAT and UVSQ INSPIRE-SAT 7.

1.6.1. *Telescope observing the Sun*

– *The context:* real-time monitoring of solar activity is necessary to better understand and predict the state of the Sun. Observation of the Lyman-alpha line enables early detection of solar flares and coronal mass ejections.

– *Applications:* research in solar physics, space weather, etc.

1.6.1.1. *Purpose of the study*

1) Study of a "disruptive" solar imaging telescope for the far ultraviolet (Lyman-alpha (121.6 nm) and Herzberg *continuum* (200–242 nm)).

2) Validation of the opto-thermal concept for the primary mirror of the SUAVE telescope (representative model). Implementation of an SIC (silicon carbide) mirror with a CVD (chemical vapor deposition) coating to minimize the effects of the space environment.

1.6.1.2. *Presentation of the optical architecture of the SODISM telescope*

The chosen optical design is shown in Figure 1.40. It is based on the definition of the SODISM telescope (see Figure 1.41), which was launched into orbit on June 15, 2010, during the PICARD mission [MEF 14].

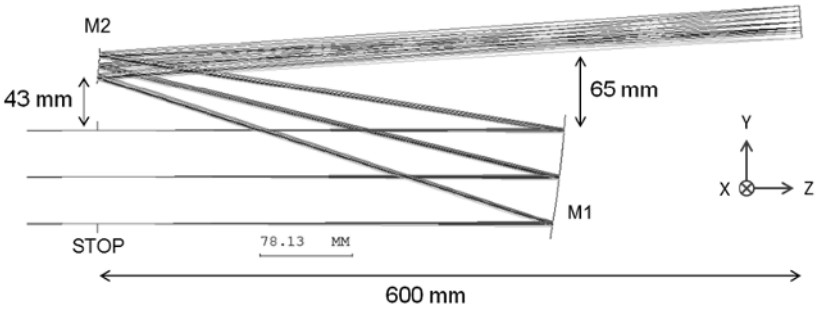

Figure 1.40. *Optical architecture of the SODISM telescope. For a color version of this figure, see www.iste.co.uk/dahoo/nanosatellites2.zip*

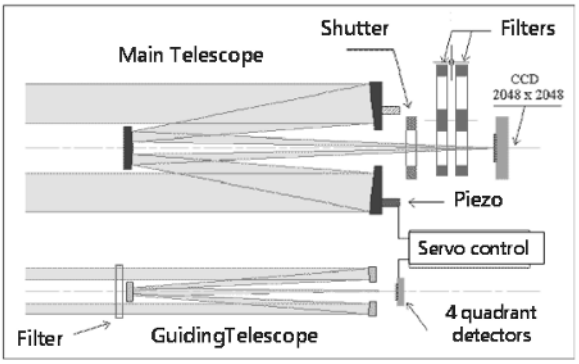

Figure 1.41. *Initial optical architecture of the SODISM telescope, PICARD mission. For a color version of this figure, see www.iste.co.uk/dahoo/nanosatellites2.zip*

BOOSTEC® SILICON CARBIDE

GENERAL	PROPERTIES	Temperature	Typical value	Unit
• Sintered SiC	*Theoritical Density*	20°C	3.21	10^3 kg/m3
	Bulk Density	20°C	3.15+/-0.05	10^3 kg/m3
• Lightweight material	*Total Porosity (fully closed)*	20°C	< 3.5	%
	Coefficient of Thermal Expansion	−200°C	0.08	10^{-6}/°C
• Outstanding thermome-chanical stability		20°C	2.2	10^{-6}/°C
		500°C	4.8	10^{-6}/°C
		1000°C	6.0	10^{-6}/°C
• High mechanical strength	*Thermal Conductivity*	−200°C	163	W/m.K
		20°C	180	W/m.K
• Excellent resistance to corrosion and abrasion		500°C	66	W/m.K
		1000°C	39	W/m.K
	Specific Heat	−200°C	42	J/kg.K
• High thermal conductivity, similar to the aluminium one		20°C	680	J/kg.K
		500°C	1040	J/kg.K
		1000°C	1180	J/kg.K
	Maximum Thermal Shock (ΔTc)		325	°C
	Maximum Temperature of Use			
	- in air		1450	°C
	- in inert atmosphere		1800	°C
	Vickers Hardness (500g load)	20°C	22	GPa
	Bending Strength: coaxial double ring	20°C		
	DIN EN 1288-1&5 Mechanical Strength		400	MPa
	Weibull Modulus		11	
	Tensile Strength	20°C	210	MPa
	Compressive Strength	20°C	3000	MPa
	K_{1C} *Toughness*	20°C	3	$MN.m^{-3/2}$
	Young's Modulus	−200 to 1000°C	420	GPa
	Shear Modulus	−200 to 1000°C	180	GPa
	Poisson's Ratio	−200 to 1000°C	0.16	
	Electrical Resistivity			
	- 0.01 V/mm	20°C / 200°C	10^5 / 10^3	Ω.m
	- 100 V/mm	20°C	10^3	Ω.m
	Emissivity	−200 to 300°C	0.7	
	Outgassing ESA ECSS-Q-70-02A			
	- TML (Total Mass Loss)		0.01	%
	- CVCM (Collected Volatile Condensable Materials)		0.00	%

Table 1.2. *Characteristics of SiC material*

A few modifications are made to keep the instrument in line with a CubeSat: an off-axis telescope, no entrance window, SIC mirrors, proper thermal control, etc. The choice of material is crucial. It is recommended to use silicon carbide (SiC)-based material to overcome the effects of degradation of Zerodur optics using metal layer deposits.

The technical characteristics of SiC shown in Table 1.2 pertain to mechanical, thermal and electrical properties. They concern theoretical density, volumetric density, porosity, thermal expansion coefficient, thermal conductivity, heat capacity or specific heat, maximum temperature supported by the material in the event of thermal shock, maximum temperature supported in air or in an inert atmosphere, supported mechanical hardness, bending strength, Weibull modulus, resistance to mechanical traction, elongation, compression resistance, hardness, Young's modulus,

shear modulus, Poisson's ratio, electrical resistance, emissivity and degassing coefficient.

Parameter	Specification	Note
Optical specifications		
Focal length	2,360 mm	
Entrance pupil diameter	80 mm	
Detector pixel	7 µm	
Field of view	+/- 0.3°	For information
Roughness	1 nm	For information (manufacture of model mirrors)
RMS diameter of image spot	< 7 µm	For all fields, at 121 nm
Spectral range	121 nm (Lyman Alpha) + 200 – 220 nm] (Herzberg continuum)	System study wavelength set at 121 nm (most restrictive wavelength)
Optical MTF at 75 cycles/mm	> 0.25	At 121 nm
Distortion	< 10 µm	Distortion calibrated on the solar disc only ⇔ +/- 0.271° field (instead of +/- 0.3° for the total field)
Reflectivity	> 40% between 120 and 220 nm per mirror	
Solar spectrum absorption	> 80%	Absorption per mirror over the entire solar spectrum

Table 1.3. *Optical characteristics of the SODISM telescope*

The specifications for the optical configuration concern the various components of the telescope's optical system, as well as the expected performance and observation range. In Table 1.3, these include the focal length of the entrance lens, the diameter of the entrance pupil, the detector pixel, the field of view, the roughness of the mirror surfaces, the rms diameter of the image spot, the spectral range covered, the optical MTF at 75 cycles/mm, the instrumental distortion, the reflectivity of the mirrors and the absorption of the solar spectrum by mirrors.

The telescope was used during the PICARD mission from 2010 to 2013. The integrated intensity of the Sun has five different wavelengths ranging from UV to near-infrared [MEF 14]. An example is shown in Figure 1.42.

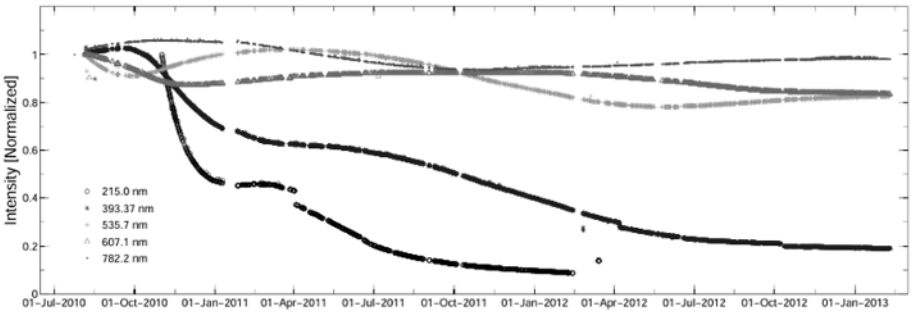

Figure 1.42. *Time series of the normalized integrated intensity of the PICARD SODISM mission: black-215 nm, blue-393 nm, green-535 nm, pink-607 nm and red-782 nm. For a color version of this figure, see www.iste.co.uk/dahoo/nanosatellites2.zip*

Parameter	M1	M2
Mechanical diameter (mm)	100	28
Useful diameter (mm	84.1	23.6
Shape	Concave	Convex
Radius of curvature (mm)	1029.855	290.749
Conicity (mm)	-0.96570	-1.94912
Offset from vertex (mm)	125.531	32.041

Mirror definition

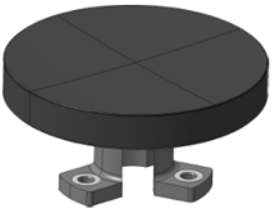

Implementation of a primary mirror with a mushroom shape

Figure 1.43. *Characteristics of the mirrors of the telescope from the PICARD SODISM mission*

The characteristics of the two mushroom-shaped mirrors (see Figure 1.40) of the telescope are shown in Figure 1.43. They pertain to the mechanical diameter, the useful diameter, the type or shape of the mirror, and the radius of curvature of the off-axis decentering.

To optimize costs, the configuration of the primary mirror is simplified. The plans for the mirror part are shown in Figure 1.44.

The optical surface of the main mirror shown in Figure 1.45 is defined by equation [1.17]:

$$Z(r) = (r^2/R)/\left(1 + \sqrt{\left(1-(1+k)\right)}(r^2/R^2)\right) \qquad [1.17]$$

with r = 1 053, k = 0 and $r^2 = x^2 + y^2$.

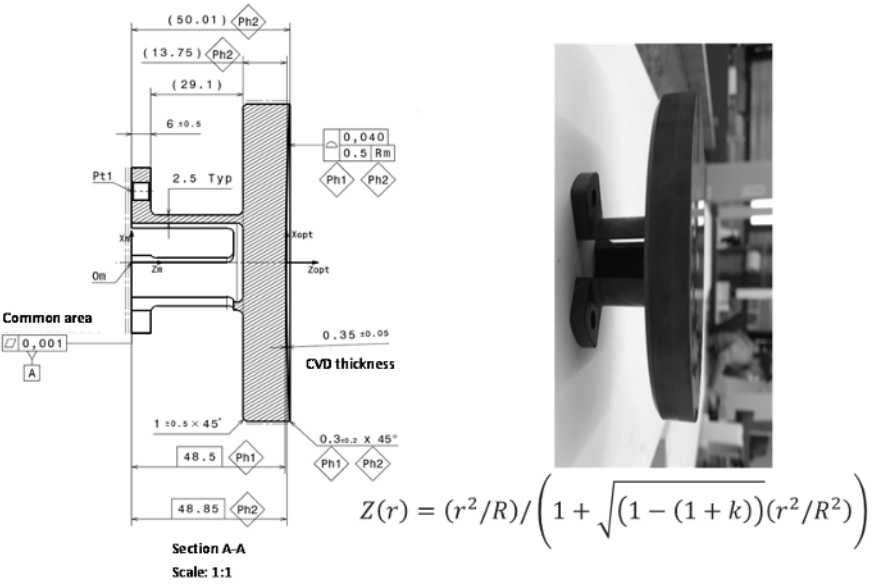

Figure 1.44. *Plans for the main mirror*

1.6.2. *Spectrometer for measuring the solar spectrum and its variability over time*

– *The context:* determining the solar spectrum and its variability over time (with a high degree of accuracy). This is fundamental data for solar physics (characterization of the activity of the Sun's outer layers), terrestrial atmospheric photochemistry and the Earth's climate.

– *Applications:* research in solar physics, study of planetary atmospheres, etc.

1.6.2.1. *Purpose of the study*

1) Implementation of a solar spectrum at a given resolution that is well known in absolute terms.

2) Development of a new miniaturized solar spectrometer.

1.6.2.2. *Presentation of the optical architecture of the SOLSPEC spectrometer*

The optical design validated is shown in Figure 1.44. It is based on the definition of the SOLSPEC (Solar Spectrometer). This instrument has made precise measurements of the SSI on board the International Space Station (ISS) in the spectral range of 165–3,000 nm [MEF 21b].

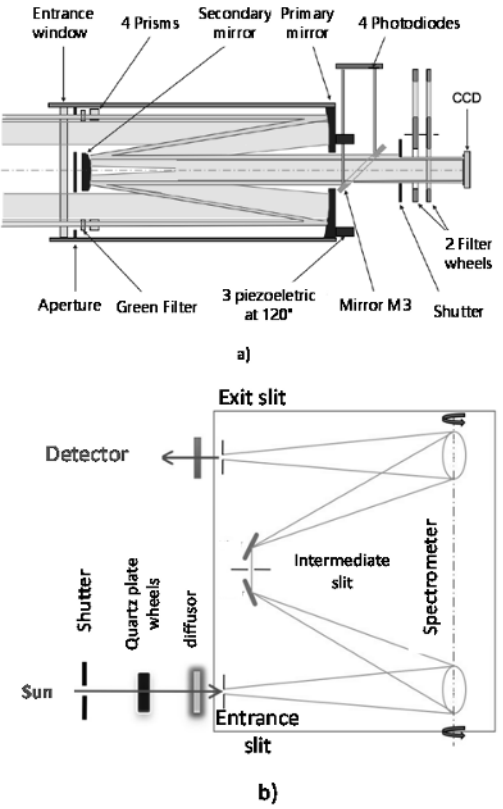

Figure 1.45. *a) SODISM configuration. b) SOLSPEC configuration. For a color version of this figure, see www.iste.co.uk/dahoo/nanosatellites2.zip*

The spectrometer was used during the campaign to measure solar irradiance at different wavelengths between April 5, 2008 and February 10, 2017. Figure 1.46 compares SOLSPEC measurements with those of the SOLSTICE, SATIRE and NRLSSI spectrometers [MEF 14].

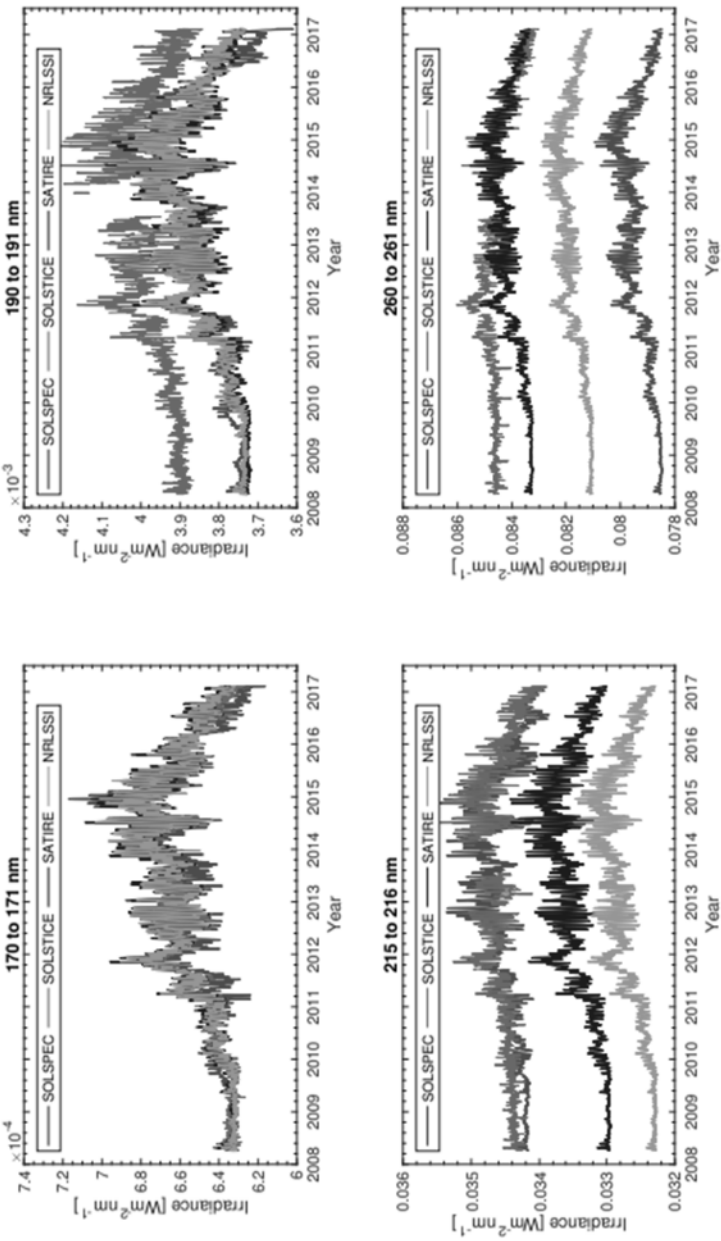

Figure 1.46. *Time series of irradiance measured with SOLSPEC aboard the ISS: 170–171 nm, 190–191 nm, 215–216 nm, 260–261 nm, and compared with measurements from SOLSTICE, SATIRE, NRLSSI [MEF 21b]. For a color version of this figure, see www.iste.co.uk/dahoo/nanosatellites2.zip*

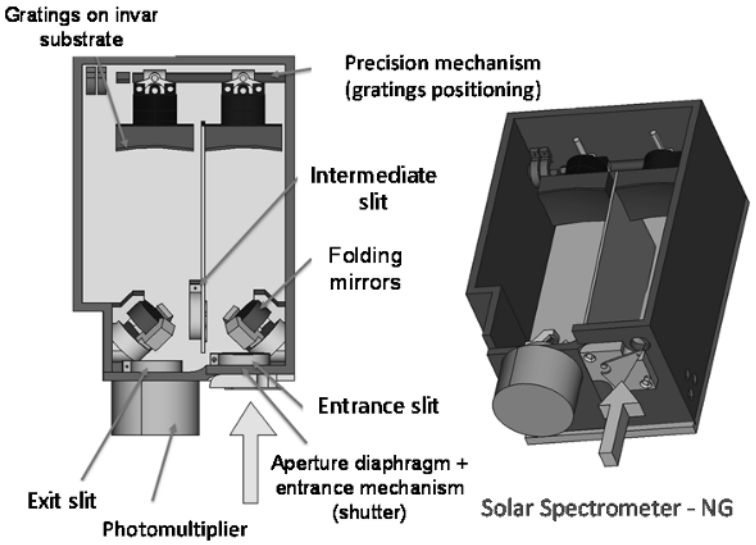

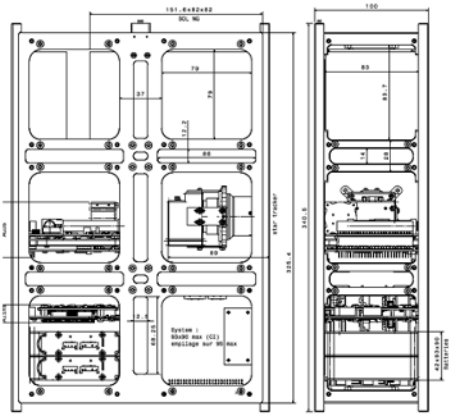

b)

Figure 1.47. *Reduced configuration of SOLSPEC for a CubeSat. For a color version of this figure, see www.iste.co.uk/dahoo/nanosatellites2.zip*

The new miniaturized configuration of the spectrometer (see Figure 1.45(b)) is shown in Figure 1.47(a) alongside the diagram of the CubeSat (see Figure 1.47(b)), on which it will carry out its measurement mission. The specific features of this configuration are given in Table 1.4.

The characteristics of the reduced spectrometer for the CubeSat mission are given in Figure 1.47.

Design #	1	2	3	4	5
Grating of toroidal type	Hologra.	Hologra.	Hologra.	Hologra.	Hologra.
Grating frequency (gr/mm)	2,000	2,000	1,000	2,000	1,000
Dimensioning length (mm)	250	200	200	100	**100**
Average FWHM (nm) @ [150-340]nm	0.5	0.6	1.2	1.0	**2.1**
Average FW10% (nm) @ [150-340]nm	0.9	1.0	2.0	1.7	**3.7**
T% max @ [150-340]nm	75.9 %	79.7 %	89.1 %	89.6 %	**94.7 %**
T% min @ [150-340]nm	51.4 %	32.9 %	91.6 %	21.9 %	**84.6 %**

Table 1.4. *Features of the reduced SOLSPEC architecture for a CubeSat*

The angular range is equal to 5.538°, and the angles are given for wavelengths of 150 nm and 340 nm as follows:

** angle = –3.159° @ 150 nm;

** angle = +2.379° @ 340 nm.

The relationship between angle and wavelength is almost linear.

The average angular step is equal to 0.02915°/nm, so that a linear calibration of wavelength according to angle would result in an error of less than ± 0.2 nm.

1.7. Conclusion

This chapter is devoted to the optical architecture of a payload and the various elements to be considered when manufacturing an optical observation instrument, whether a telescope or a spectrometer, for measurement and observation missions on a CubeSat. These have been described in the context of theories developed to explain how light phenomena occur and behave and how to build instruments to increase our ability to observe, be it small objects or those located far away in deep space. The introduction provided a historical overview of the progress made since the pioneers who paved the way for modern science, focusing in particular on the theories of

geometric optics and wave optics. Wave phenomena were also presented in the context of Maxwell's equations for propagation and radiation phenomena. Quantum optics was presented in the context of light–matter interaction for detection systems such as the photoelectric effect. The various sources of error in optical instrumentation were presented in order to clearly demonstrate the extent to which it is necessary to reduce sources of error. These include aberration phenomena, deviations from the Gaussian approximation (Gaussian optics) in geometric optics, diffraction, aperture effects on spatial frequencies in Fourier optics and nonlinearity or saturation effects related to sensor properties. Two examples of optical instruments that have been adapted, and which have already demonstrated how well they work on instruments bigger than nanosatellites, are shown at the end of the chapter to show how to adapt and design the optical payload for CubeSat missions.

1.8. Appendix

1.8.1. *Propagation of light in wave optics*

In light diffraction problems, we seek to deduce the amplitude of a wave $E_z(x,y)$ located in a plane z from the amplitude $E_0(x,y)$ of a wave located in the plane z = 0.

In Chapter 3 of reference [DAH 16], equation [3.6] gives the expression of an electromagnetic wave traveling along Oz in the form u(z-vt) = acos(k(z-vt)), where v is the propagation speed of the wave in a medium with index n (n = c/v), a is its amplitude and k = 2π/λ. In a vacuum, n = 1, and if we consider a three-dimensional space, we can express the monochromatic plane wave with frequency ω = kc and wave vector $\mathbf{k} = (k_x, k_y, k_z)$ in complex notation as $\mathbf{E} = \mathbf{E_0} \exp i(2\pi/\lambda\ (\alpha x+\beta y+\gamma z) - \omega t)$, where the components of the wave vector are in the form: $k_x = 2\pi\alpha/\lambda$, $k_y = 2\pi\beta/\lambda$ and $k_x = 2\pi\gamma/\lambda$, α, β, y being the direction cosines of the wave vector **k** and λ being the wavelength.

This expression can be obtained by solving the Helmholtz equation ([3.7] in [DAH 16]):

$$\Delta\vec{E} + \frac{\omega^2}{c^2}\vec{E} = \vec{0} \qquad [1.18]$$

where $\Delta\vec{E} = \vec{\nabla}^2\vec{E}$.

The propagation of a wave through obstacles (transparent apertures or opaque objects) can be determined using Green–Ostrogradski's theorem and the Green function $G_k(\vec{r},\vec{r}_0)$ of the Helmholtz equation, which is written as $G_k(\vec{r},\vec{r}_0) = -\frac{exp(ik|\vec{r}-\vec{r}_0|)}{4\pi|\vec{r}-\vec{r}_0|}$. Here, the surface integral surrounds the point marked by $\vec{r}_0$, where we

are looking for the electric field $\vec{E}(\vec{r}_0)$ and $\vec{r}$ is the position of the element $d\vec{s}$ of the transparent aperture or obstacle.

At a large distance compared to the wavelength such that $k|\vec{r} - \vec{r}_0| \gg 1$, we obtain the solution:

$$\vec{E}(\vec{r}_0) = \oint \left(\vec{E}(\vec{r}) \left\{ \frac{ik}{|\vec{r} - \vec{r}_0|} (\vec{r} - \vec{r}_0) G_k(\vec{r}, \vec{r}_0) d\vec{s} - ikG_k(\vec{r}, \vec{r}_0) ds \right\} \right) \quad [1.19]$$

hence:

$$\vec{E}(\vec{r}_0) = -\frac{ik}{4\pi} \oint \vec{E}(\vec{r}) \frac{exp(ik|\vec{r} - \vec{r}_0|)}{|\vec{r} - \vec{r}_0|^2} \left((\vec{r} - \vec{r}_0) d\vec{s} - |\vec{r} - \vec{r}_0| ds \right) \quad [1.20]$$

This solution corresponds to the formulation of the Huygens–Fresnel principle or the Huygens–Fresnel equation obtained by Kirchhoff's integral. This is the Fresnel–Kirchhoff diffraction formula.

Detailed calculations justifying the Huygens–Fresnel principle through the application of the Fresnel–Kirchhoff integral can be found in reference [BOR 99], along with optical assembly diagrams specifying the direction of the normals to the diffracting surfaces for the scalar wave.

When a plane, monochromatic wave propagating parallel to Oz encounters a screen (E_0) with an aperture (see Figure 1.48), a diffraction pattern is formed in the observation plane. For simplicity, we assume that the plane of the aperture is perpendicular to the propagation of the plane wave and that the amplitude and gradient of the wave's electric field are constant over the surface of the aperture only in the vicinity of a point M on the surface.

The amplitude on the other side of the aperture at a point P marked by $\vec{r}_0$ is given by the Fresnel–Kirchhoff diffraction formula. If the aperture is in the Oxy plane (see Figure 1.48) and the dimensions are small compared to the position of point P at $\vec{r}_0$, the amplitude of the field at P is obtained as follows:

$$\vec{E}(\vec{r}_0) = -\frac{ik\vec{E}(\vec{r})}{4\pi R} (cos\theta + 1) \oint exp(ik|\vec{r} - \vec{r}_0|) dxdy \quad [1.21]$$

where R is the distance between the center point of the aperture and point P (as a first approximation, this is the same distance for all points on the aperture), and θ is the angle between the Oz axis and the vector $\overrightarrow{MP} = \vec{r}_0 - \vec{r}$. The origin of the coordinates is taken in the plane containing the diffracting aperture.

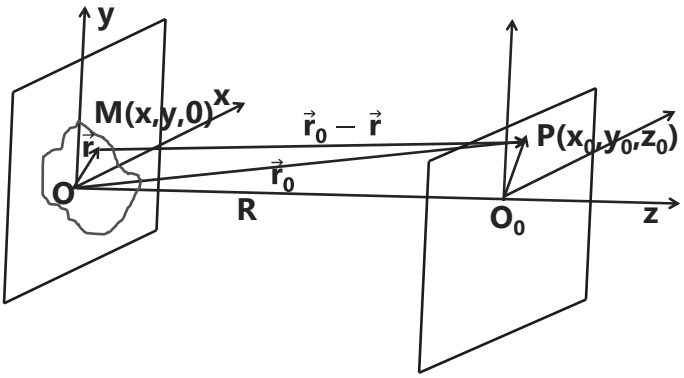

Figure 1.48. *Diagram showing diffraction in a plane containing P by an aperture containing M*

The modulus of the vector $\vec{r}_0 - \vec{r}$ is given by $|\vec{r}_0 - \vec{r}| = \sqrt{r_0^2 - 2\vec{r}_0.\vec{r} + r^2}$.

In [BOR 99], the scalar wave $V(x,y,z,t) = U(x,y,z)exp(-i\omega t)$, where $U(x,y,z)$ is the solution to the Helmholtz equation corresponding to a monochromatic wave. For a polychromatic wave, it is given in the form of a Fourier integral:

$$V(x,y,z,t) = \frac{1}{\sqrt{2\pi}}\int_{-\infty}^{\infty} U_\omega(x,y,z)exp(-i\omega t)d\omega \quad [1.22]$$

which allows us to write, using the inverse Fourier transform, that $U_\omega(x,y,z)$ is given by:

$$U_\omega(x,y,z) = \frac{1}{\sqrt{2\pi}}\int_{-\infty}^{\infty} V(x,y,z,t)exp(+i\omega t)dt \quad [1.23]$$

where $U_\omega(x,y,z)$ is the solution to the Helmholtz equation, which is expressed as:

$$U_\omega(x,y,z) = \frac{1}{4\pi}\oint\left\{U_\omega\frac{\partial}{\partial n}\left(\frac{\exp(iks)}{s}\right) - \frac{\exp(iks)}{s}\frac{\partial U_\omega}{\partial n}\right\}dS \quad [1.24]$$

where s is the distance between a point (x, y, z) on the closed surface S and a point P inside the volume bounded by the closed surface S where the amplitude of the diffracted wave is calculated.

After integration, in this case we calculate the amplitude of the wave at point P, which is given by the following integral:

$$V(x,y,z,t) = \frac{1}{4\pi}\iint_{Smin}^{Smax}\left\{[V]\frac{\partial}{\partial n}\left(\frac{1}{s}\right) - \frac{1}{cs}\frac{\partial s}{\partial n}\left[\frac{\partial V}{\partial t}\right] - \frac{1}{s}\left[\frac{\partial V}{\partial n}\right]\right\}\mathrm{dS} \quad [1.25]$$

where the terms in square brackets represent retarded quantities whose values are taken at time t-s/c, V, a solution of the wave equation in the time domain being given by formula [1.22]. This formula is the general form of Kirchhoff's theorem for a polychromatic wave.

The reference [BOR 99] provides detailed calculations concerning the justification of Huygens–Fresnel's principle. This can be done by applying the Fresnel–Kirchhoff integral or Rayleigh–Sommerfeld integrals of the first kind (which correspond to the Dirichlet boundary conditions pertaining to the value of the amplitude of the plane wave) and second kind (which corresponds to the Neumann boundary conditions pertaining to the value of the gradient of the plane wave amplitude).

If we consider the conditions of the Fraunhofer diffraction in the far field, with an origin O in the plane of the aperture (see Figure 1.48), where R is the distance between the observation plane and the diffracting plane, we can write that:

$$exp(ik|\vec{r} - \vec{r}_0|) = exp\left(ik\sqrt{r_0^2 - 2\vec{r}_0.\vec{r} + r^2}\right) = e^{ikR}exp\big(-ik(\alpha x + \beta y)\big) \quad [1.26]$$

where $\alpha = \frac{x_0}{R}$ and $\beta = \frac{y_0}{R}$ with $\vec{r}_0 = R\vec{u}_z + x_0\vec{u}_x + y_0\vec{u}_y$ and $\vec{r} = x\vec{u}_x + y\vec{u}_y$.

In the case of the Gaussian approximation, with paraxial rays, we obtain for the field at P:

$$\vec{\mathrm{E}}(\vec{r}_0) = \mathrm{A}\iint exp\big(-ik(\alpha x + \beta y)\big)dxdy \quad [1.27]$$

Fraunhofer diffraction at a large distance can thus be calculated using this formula, which corresponds to the Fourier transform of the transparency function t(*x,y*) of the aperture containing point M.

The illumination at the coordinates marked by the vector $\vec{r}_0$ is written as:

$$\vec{\mathrm{E}}(\vec{r}_0) = \iint \mathrm{A}t(x,y)exp\left(-i\frac{2\pi}{\lambda}(\alpha x + \beta y)\right)dxdy \quad [1.28]$$

where A is the amplitude of the incident wave in the aperture plane. This expression corresponds to the Fourier transform of $t(x,y)$. The variables $\frac{x_0}{R} = \frac{\alpha}{\lambda}$ and $\frac{y_0}{R} = \frac{\beta}{\lambda}$ are

the conjugate spatial frequencies of the space variables (x, y) located in the object plane.

The field of wave optics that deals with the Fourier transform of illuminated objects in relation to space is called Fourier optics. Thus, by selecting spatial components of an image, spatial filtering is performed to modify and improve the quality of an image received, for example, by a 2D detector. Since the Fraunhofer diffraction is performed for a point located at infinity, a converging lens is used to bring this point to a finite distance on a screen.

1.8.1.1. *Image processing*

When studying images of objects that are not point sources, we can use the object's Fourier transform to determine its image focused on a screen, according to the method developed by Duffieux (1891–1976) [DUF 46, DUF 45].

The Fourier transform is a mathematical operation that consists of decomposing a function according to its frequencies. There are different formulations of a function's Fourier transform.

Usually, we calculate the Fourier transform F(ν) of a time signal f(t), which is given by the expression:

$$F(\nu) = \int_{-\infty}^{+\infty} f(t) exp(-i2\pi\nu t) dt \qquad [1.29]$$

The inverse Fourier transform allows determination of f(t) by:

$$f(t) = \int_{-\infty}^{+\infty} F(\nu) exp(+i2\pi\nu t) d\nu \qquad [1.30]$$

The two functions $f(t)$ and $F(\nu)$ play symmetrical roles, one function being the spectrum of the other.

If we consider a function with two variables f(x,y), the Fourier transform is written as follows:

$$F(\mu, \nu) = \iint_{-\infty}^{+\infty} f(x, y) exp(-i2\pi(\mu x + \nu y)) dx dy \qquad [1.31]$$

and the inverse Fourier transform as follows:

$$f(x, y) = \iint_{-\infty}^{+\infty} F(\mu, \nu) exp(+i2\pi(\mu x + \nu y)) d\mu d\nu \qquad [1.32]$$

Setting $\frac{\alpha}{\lambda} = \mu$ and $\frac{\beta}{\lambda} = \nu$, the illuminance at the coordinates marked by vector $\vec{r}_0$ (formula [1.28]) is written as:

$$F(\mu, \nu) = \mathrm{A} \iint \mathrm{f(x,y)} exp(-i2\pi(\mu x + \nu y)) dxdy \qquad [1.33]$$

where f(x,y) = $t(x, y)$ and A is the amplitude of the incident wave in the plane of the aperture. This expression corresponds to the Fourier transform of $f(x, y)$. The variables μ, ν are the conjugate spatial frequencies of the space variables (x, y) located in the object plane.

1.8.2. *Terrestrial radiation sensors*

1.8.2.1. *Measuring incoming solar irradiance*

To accurately measure terrestrial solar irradiance (TSI) and outgoing terrestrial radiation (OLR and OSR), new ERS (Earth Radiation Sensor), or miniaturized thermopile sensors, have been developed. The assembly of the ERS is shown in Figure 1.49. The ERS have an active surface area of 5 mm × 5 mm and a sensitivity of approximately 0.2 μV/Wm^{-2}, designed to measure the thermal flux of a surface covering a field of view angle of 180°.

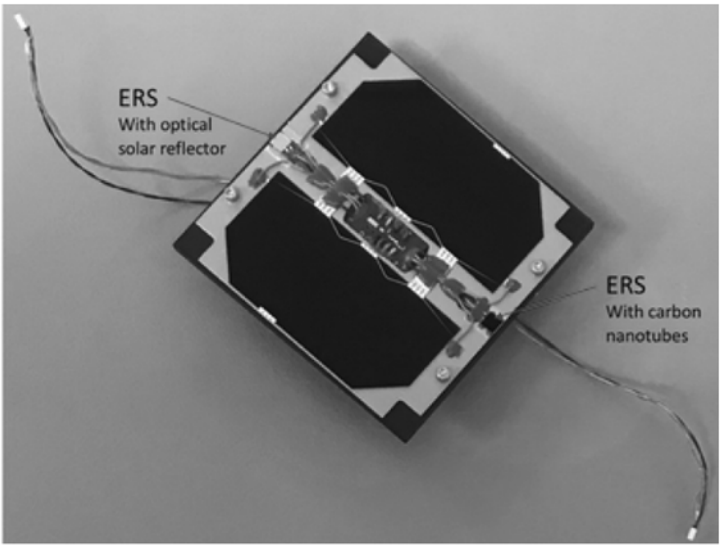

Figure 1.49. *Miniaturized thermopile ERS sensors*

The passive (cold) junctions of the thermopile are completely enclosed in a structure to protect them from radiation, which also serves as a heat sink. The measurement principle of these sensors is shown in Figure 1.49. Carbon nanotube ERS and optical solar reflector ERS are equipped on each side of the UVSQ-SAT CubeSat (see Figure 1.50).

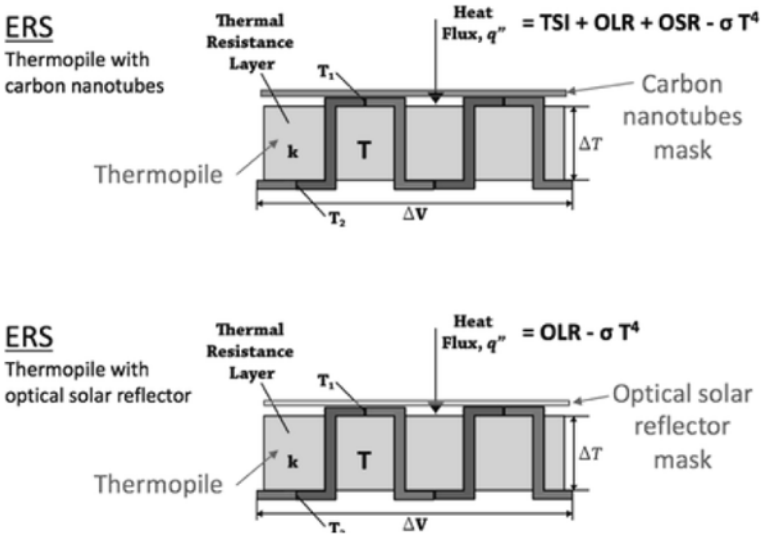

Figure 1.50. *Carbon nanotube ERS and optical solar reflector ERS. For a color version of this figure, see www.iste.co.uk/dahoo/nanosatellites2.zip*

The carbon nanotubes present in ERS will absorb all incoming solar radiation and outgoing terrestrial radiation. Their spectrum is flat from UV to 100 μm and their cosine response is almost perfect. Among the darkest materials, carbon nanotubes (Vantablack – Surrey NanoSystems) can absorb 96.964% of the light at 700 nm that passes through them when it is perpendicular to the tube. The performance of the bidirectional reflectance distribution function (BRDF) of these carbon nanotubes has been demonstrated for a range of incidence angles (see Figure 1.51) and scattering angles (total integrated scattering of 0.94% at an incidence angle of 70°). ERS will primarily absorb long-wave radiation from the upper atmosphere via optical solar reflectors. They have high reflectance of UV radiation up to 3 μm. They were selected because the variation in solar absorption due to environmental exposure (thermal cycling, UV radiation, protons, etc.) is extremely low.

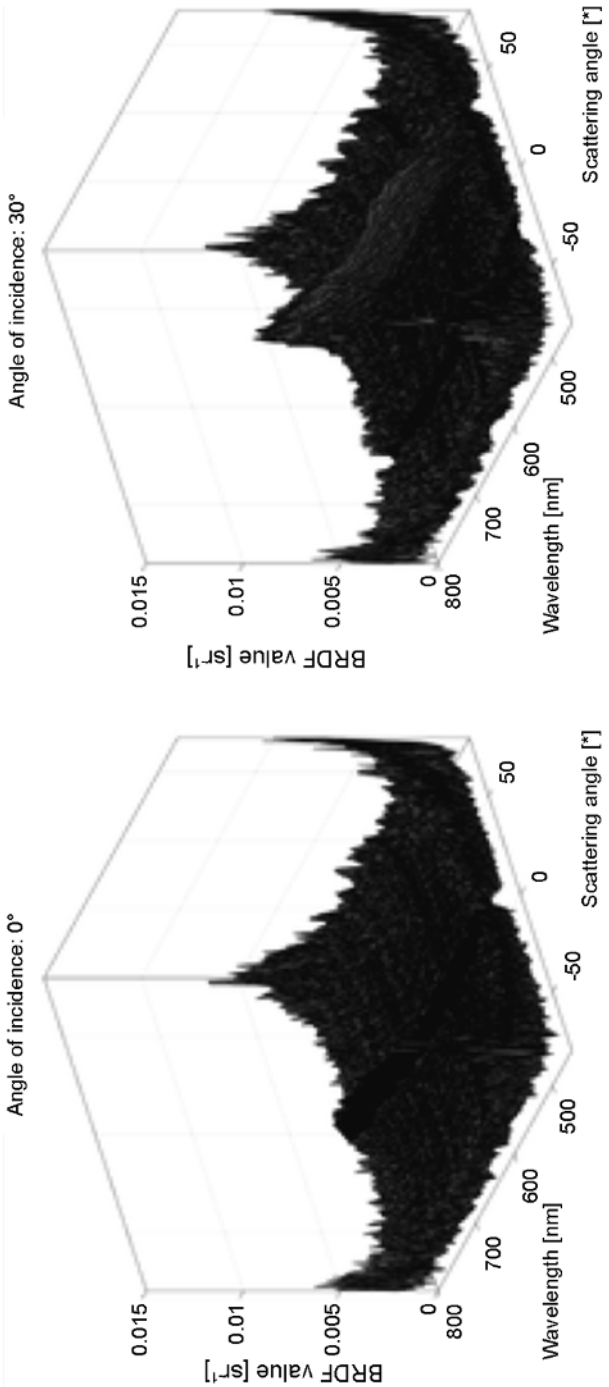

Figure 1.51. *Bidirectional reflectance distribution function (BRDF)*

The performance of the coatings (carbon nanotubes and optical solar reflectors) is measured using a spectrophotometer (Agilent – Cary 5000 UV–Vis–NIR) to obtain solar absorption (between 200 and 2,500 nm), an IR reflectometer (model DB100) to obtain normal IR emissivity (approximately 10 μm) and a goniophotometer (REFLET 180S) to obtain the BRDF (five angles of incidence (0, 30, 36, 60 and 72°) in the wavelength range from 400 to 800 nm in 10 nm increments).

The wide field of view of the two sensors on either side of UVSQ-SAT allows for the measurement of all fluxes (TSI, OLR, OSR, black body flux of the sensor (σT^4), residual fluxes (Moon, planets, etc.)). Given that we know the value of solar flux (TSI measurement obtained from space-based solar radiometers), the sensor temperatures (UVSQ-SAT housekeeping data) and the residual fluxes (ephemerides of various bodies in the Solar System obtained from the French Institute of Celestial Mechanics and Ephemeris Computation (IMCCE)), we can determine OLR and OSR from a system of two equations.

1.8.2.2. *UVS and TSIS sensors*

A new optical system (UVS) based on a Hamamatsu Si photodiode, which accurately measures solar spectrum irradiation in the Herzberg continuum (200–242 nm), has been developed for UVSQ-SAT. Three TSIS sensors, which measure solar irradiance in the range of 200–1,100 nm, have also been developed. Figure 1.52 shows the optical assembly used for the UVS and TSIS sensors.

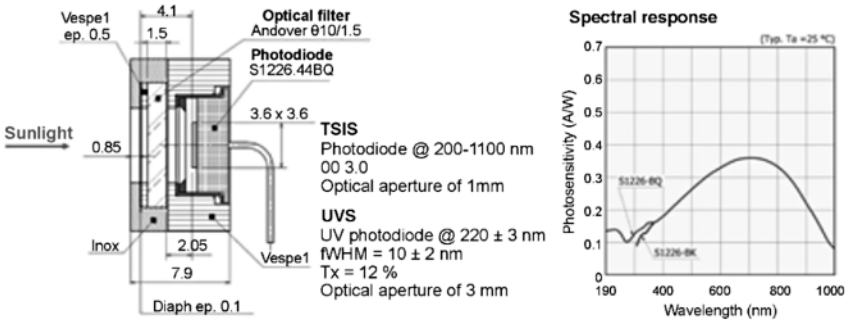

Figure 1.52. *The optical system used for UVS and TSIS sensors. For a color version of this figure, see www.iste.co.uk/dahoo/nanosatellites2.zip*